Petroleum Science 23 (2026) 5203–5220

Contents lists available at ScienceDirect

Petroleum Science

journal homepage: www.keaipublishing.com/en/journals/petroleum-science

Original Paper

Study on the pyrolysis of kerogen at varying moisture contents: Experimental modeling and ReaxFF simulation

Yue-Qin Li [a], Wen-Ji-Bin Sun [a,*], Yu-Jun Zuo [a], Bo-Bo Li [a], Zhong-Hu Wu [b], Lei Zhang [c], Ren-Jun Tian [d], Wei Lv [a]

[a] Mining College, Guizhou University, Guiyang, 550025, Guizhou, China
[b] College of Civil Engineering, Guizhou University, Guiyang, 550025, Guizhou, China
[c] School of Mines, China University of Mining and Technology, Xuzhou, 221116, Jiangsu, China
[d] School of Resource and Environmental Engineering, Guizhou University, Guiyang, 550025, Guizhou, China

ARTICLE INFO

Article history:
Received 3 July 2025
Received in revised form
10 December 2025
Accepted 6 March 2026
Available online 11 March 2026

Edited by Min Li

Keywords:
Shale
Hydrous pyrolysis
Molecular structure
ReaxFF MD
Free radical

ABSTRACT

Hydrocarbon generation from shale usually occurs in a reducing aqueous environment. Understanding the pyrolysis characteristics of shale kerogen under hydrous conditions is crucial for elucidating the hydrocarbon generation mechanism, yet few microscale studies have examined how varying moisture content affects shale pyrolysis. This study characterizes the microstructure of shale kerogen samples and performs hydrous pyrolysis simulations using ReaxFF MD technology. The results indicate that hydrous pyrolysis promotes the cracking of kerogen and increases the yield of gaseous hydrocarbons. Water significantly increases the types and numbers of free radicals during the pyrolysis process, enhances reaction activity, facilitates dehydrogenation reactions, and improves the saturation of kerogen molecules. The degree of aromatic condensation in kerogen determines the optimal moisture content threshold for promoting pyrolysis, while the presence of polar functional groups shifts this threshold. As the degree of aromatic ring condensation increases, the hydrophobicity of kerogen increases, thereby raising the optimal moisture content threshold for promoting pyrolysis. At low moisture content, water has minimal effect on pyrolysis and may even inhibit the reaction. Moreover, the yields of gaseous hydrocarbons and char from kerogen are positively correlated with the concentration of hydrogen free radicals (·H). These findings provide a theoretical foundation for shale gas exploration and development.

1. Introduction

The increasing demand for energy and the continuing depletion of oil resources have prompted several countries to explore alternative sources. With abundant reserves and huge exploitation potential, shale gas has become an important supplementary source of conventional natural gas (Hou et al., 2025; Roshan et al., 2016; Wang et al., 2023b). Studying the mechanisms of gas generation from organic matter during the cracking process is crucial for shale gas exploration, production forecasting, and efficient extraction (Wang et al., 2016). Kerogen is the primary organic component in sedimentary rocks (Babaei et al., 2023). It undergoes thermal evolution and microbial transformation over geological timescales, leading to the formation of shale gas. The pyrolysis of kerogen to produce hydrocarbons is regulated by the coupling of multiple factors, including temperature (Wang et al., 2023a), pressure (Meng et al., 2024; Zhang et al., 2024), and water medium (Zheng et al., 2023).

The deposition and hydrocarbon generation of shale occur in the reducing environment of water (Cheng et al., 2019; Zhang et al., 2019a). Water acts as a key inorganic donor, providing external hydrogen to over-mature source rocks (Cheng et al., 2019). Simple anhydrous pyrolysis at high temperatures cannot fully simulate the natural maturation process (Siskin and Katritzky, 1991). The goal of artificial maturation of organic matter should be to approximate or simulate natural processes (Lindsey et al., 2023). After the proposal of the hydrous pyrolysis artificial maturation method (Lewan et al., 1979), simulating the water-rock interaction during the thermal maturation of organic matter provides maturity data that highly consistent with the natural process (Behar

* Corresponding author.
E-mail address: sunwenjibin@163.com (W.-J.-B. Sun).
Peer review under the responsibility of China University of Petroleum (Beijing).

https://doi.org/10.1016/j.petsci.2026.03.012

et al., 2003; Zheng et al., 2023). Nevertheless, the effect of water molecules on kerogen pyrolysis remains controversial. Early hydrous pyrolysis experiments suggest that kerogen pyrolysis is inhibited in water-rich environments compared to closed, anhydrous pyrolysis (Michels et al., 1995), but subsequent studies reveal that water not only participates as a reaction medium, but also its hydrogen atom is more directly involved in the formation of hydrocarbons (Li et al., 2022b). Importantly, the catalytic effect of water is maturity-dependent. At low maturity stages (R_o < 1.0%), water has minimal impact on C_1–C_4 gaseous hydrocarbon yields (Lewan, 1997; Wang et al., 2011), whereas at high maturity stages (R_o > 1.3%), it significantly enhances gaseous hydrocarbon production (Gao et al., 2020). In extraction processes, the hydrocarbon yield from some shale gas wells exceeds the predicted range of conventional source rock maturity models. This may be due to conventional source rock maturity models limiting hydrocarbon generation to the amount of organically bound hydrogen. In practical processes, however, kerogen may be hydrogenated by water (Wang et al., 2022a). While considerable research has been conducted on shale pyrolysis mechanisms, most previous hydrous pyrolysis experiments have been from a macroscopic perspective. Using hydrous pyrolysis devices, rock samples are kept in contact with liquid water at liquid-gas equilibrium pressure or high pressure. Techniques such as μ-FTIR, CP-Py-GC/MS, and BIB-SEM-EDS (Zheng et al., 2023), or isotopic labeling tracking experiments (Li et al., 2022b), are used to analyze the chemical evolution of kerogen under hydrous pyrolysis. Despite these advances, the quantitative effect of the moisture content gradient on pyrolysis kinetics at the nanoscale still lacks a molecular mechanism explanation.

Shale pyrolysis is a complex process driven by free radicals, involving numerous highly reactive and short-lived free radical intermediates (Salmon et al., 2009). It is difficult to capture the formation details of these intermediates by experimental methods. Reaction force field molecular dynamics (ReaxFF MD) simulation is an effective method to explore complex reactions in macromolecular systems from a microscopic perspective (Huang et al., 2023;Li et al., 2022a). This simulation method enables the study of the thermal cracking of organic materials without requiring assumptions about the reaction mechanism (Salmon et al., 2009). Lately, ReaxFF has been applied extensively to investigate the reaction processes of coal (Liu et al., 2024; Qiu et al., 2022), oil shale (Chen et al., 2023; Wang et al., 2019; Wang et al., 2023a), and other organic materials. Some scholars have studied the effect of water vapor on the in-situ pyrolysis products of kerogen using the ReaxFF force field. These studies indicate that water vapor inhibits the dehydrogenation reactions of kerogen, enhances the saturation of hydrocarbon products, and facilitates the removal of heteroatoms such as sulfur and nitrogen (Zhao et al., 2022, 2023). Furthermore, hydrogen free radicals in the water vapor suppress cross-linking reactions between small fraction products, thereby reducing the average molecular weight of the organic molecular products (Zhang et al., 2021). However, the hydrocarbon generation behavior during the thermal evolution of marine shale kerogen with different degrees of aromatic condensation under hydrous conditions has not been systematically investigated (Liu et al., 2024; Zheng et al., 2023). Therefore, it is necessary to carry out a comparative study on the pyrolysis behavior of shale kerogen with different aromatic condensation degrees under the control of moisture content gradient based on nano-scale characterization technology. This research is valuable for understanding the coupling effect between kerogen structure and moisture content conditions on hydrocarbon generation.

The Sichuan Basin is the most extensively studied region for the molecular structure of source rocks in southern China. Using techniques such as Fourier transform infrared spectroscopy (FTIR), X-ray photoelectron spectroscopy (XPS), and solid-state ^{13}C nuclear magnetic resonance (^{13}C NMR), models of Silurian and Cambrian kerogen have been constructed, revealing their low nitrogen and sulfur content and high thermal maturity (Hou et al., 2023; Huang et al., 2018; Li et al., 2025; Yang et al., 2025a). In contrast to the Sichuan Basin, molecular structure modeling and microstructure studies of the Longmaxi Formation in Guizhou are relatively limited. Accordingly, this study focuses on the Longmaxi Formation in Guizhou as the research object, using techniques such as elemental analysis (EA), ^{13}C NMR, FTIR, and XPS to characterize the microstructure of kerogen samples from the Guizhou Longmaxi Formation (Han et al., 2023; Hu et al., 2024). The experimental data is then used to create an empirical kerogen molecular model, and the model's rationality is evaluated through density and pair distribution function (PDF) calculations. Finally, based on the reaction force field, the pyrolysis process of kerogen under the coupling of structure and hydrous conditions is discussed and analyzed to better understand the pyrolysis hydrocarbon generation mechanism of marine shale kerogen. This understanding can help more accurately predict the location of shale gas desserts and the types of hydrocarbons produced, reducing the uncertainty in resource assessment. The schematic steps of this study are depicted in Fig. 1.

2. Experimental

2.1. Material preparation

The AY1-6 and AY2 shale core samples are collected from the Silurian Longmaxi Formation in northern Guizhou, China, with burial depths ranging from 100 to 2500 m and thicknesses varying between 30 and 120 m. The total organic carbon (TOC) content of the samples is measured using a German-made Elementar vario TOC select carbon/sulfur analyzer. The TOC content of AY1-6 and AY2 is 5.23 wt.% and 2.61 wt.%, respectively. The corresponding kerogen is isolated by chemical dissolution of minerals.

The two main acids that are utilized to dissolve the mineral components are hydrochloric acid (HCl) and hydrofluoric acid (HF). Because no organic solvents are utilized, the kerogen samples retain tiny organic compounds like asphaltenes. HF and HCl are added to the samples, followed by heating and stirring in a heated stirrer. The mineral components are removed using a centrifuge. EA is used to determine the samples' elemental composition. Table 1 displays the TOC content of the Longmaxi shale, along with the corresponding kerogen element analysis results.

2.2. Characterization

2.2.1. FTIR

FTIR spectra of the kerogens, ranging from 4000 to 400 cm^{-1}, are obtained using KBr pellet technology on a Thermo Fisher Scientific Nicolet iS20 spectrometer. A total of 64 scans is conducted with a spectral resolution of 4 cm^{-1}. This method is employed for the preliminary assessment of functional group distribution. As noted by Iglesias et al. (1995), the degradation or collapse of functional group bands in samples with higher thermal maturity may lead to very small peak areas, introducing uncertainty in peak area measurements. In this study, the infrared experiments are primarily conducted for qualitative analysis. The FTIR spectra are baseline-corrected, and the positions and numbers of the spectral bands are determined by analyzing the second derivative spectrum (Painter et al., 1981). Gaussian fitting of the experimental

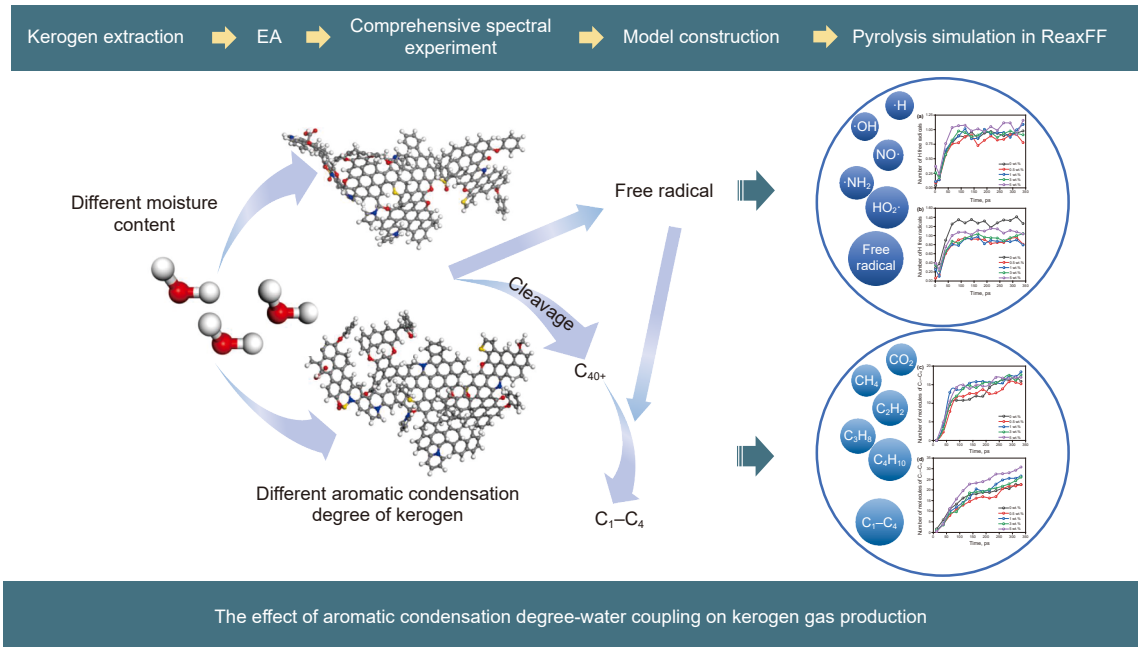

Fig. 1. Schematic diagram of the research process.

Table 1
The TOC content and kerogen element content of AY1-6 and AY2.

Sample	Element, wt.%					Atomic ratio		TOC, wt.%
	C	H	O	N	S	H/C	O/C	
AY1-6	78.26	2.80	4.98	1.80	2.01	0.43	0.05	5.23
AY2	78.46	2.72	4.88	1.82	2.28	0.43	0.05	2.61

curves is then conducted using ORIGIN 2021 software (Hou et al., 2023; Painter et al., 1981).

2.2.2. XPS

The XPS analysis of the kerogen samples is conducted using the Thermo Scientific K-Alpha XPS device. A monochromatic aluminum anode (Al Kα) is used as the source gun. The binding energy is calibrated using the carbon (1s) peak at 284.8 eV (Pinder et al., 2024; Wang et al., 2024). The types and contents of oxygen elements are calculated from the XPS carbon (1s) signal of adjacent carbon atoms (Pan et al., 2022). Curve fitting is applied to the narrow scan peaks of C1s, N1s, and S2p to define and quantify the morphology of heteroatom functional groups in kerogen samples. The binding energy distributions of the element peaks are referenced from the literature (Kelemen et al., 2007; Su et al., 2024). Single peak fitting is used for the analysis of the C1s and N1s elements. However, due to the susceptibility of the S2p electrons to energy level splitting under X-ray excitation during the XPS test, a double peak fitting approach is used to improve the accuracy of sulfur element fitting (Wang et al., 2019). Specifically, the S2p analysis is carried out using a single peak for $2p_{3/2}$ and its split peak for $2p_{1/2}$. The peak area ratio of $2p_{3/2}$ to the split peak $2p_{1/2}$ is 2:1, with a splitting distance of 1.2 ($\pm$0.1) eV. During the fitting process, the Shirley model is used for background subtraction, and a 70% Gaussian-30% Lorentzian mixed line shape is applied.

2.2.3. Solid-state ^{13}C NMR

Due to the low hydrogen content of this sample, solid-state dipolar decoupling magic angle spinning (DD/MAS) ^{13}C NMR testing is conducted using the ECZL600G instrument (Japan Electronics). The signal from adamantane is used as the reference for the ^{13}C chemical shift, and the experimental curve fitting involved Lorentzian/Gaussian contributions. The measurement conditions are as follows: a single-pulse decoupling method with a resonance frequency of 150.762 MHz is employed. A 3.2 mm HX dual-resonance probe and rotor are used. The test speed is 15 kHz, with a spectral width of 56.82 kHz and a relaxation delay of 1 s. The acquisition time is 22.53 ms.

2.3. Simulation procedure

2.3.1. Model construction

The chemical structure model forms the foundation for studying the thermal evolution of kerogen. Currently, a relatively comprehensive kerogen modeling system has been established and applied in numerous studies (Chen et al., 2026; Liu et al., 2021; Trewhella et al., 1986). The reconstruction of the chemical structure of Longmaxi shale kerogen primarily depends on experimental characterization results from techniques such as ^{13}C NMR and XPS, supplemented by FTIR spectroscopy for the qualitative verification of functional groups, such as carbonyl (–C=O). To construct an accurate kerogen model, five organic elements carbon (C), hydrogen (H), oxygen (O), nitrogen (N) and sulfur (S) are considered.

Moisture content (wt.%) is defined as the mass ratio of the molecular mass of water to the kerogen skeleton mass, which is used to describe the moisture content in organic matter. Five moisture content groups (0, 0.5, 1, 3, 5 wt.%) are set. Based on the constructed kerogen and water molecular models, a specified number of water molecules and 10 kerogen molecules are placed into a periodic cell system with an initial density of 0.1 g/cm^3, corresponding to the defined moisture content. The PCFF force field is applied with a cutoff distance of 1.0 Å, and the PPPM method is used to calculate long-range Coulomb interactions with an accuracy of 1×10^{-4}. The time step is set to 1 fs. The simulation is initially conducted at 2000 K using an NVT ensemble, with the system controlled by a Nose-Hoover thermostat and a damping constant of 100 fs. The simulation duration is 300 ps.

Subsequently, a cooling relaxation from 2000 to 300 K is performed under the NPT ensemble to achieve the target density, with the pressure set to 30 MPa. The simulation time for this step is 200 ps. If the density does not fall within the desired range, the relaxation process is repeated. Once the system reaches a reasonable density range, an additional NVT relaxation at 300 K is carried out for 300 ps to further relax the model. During this process, the energy and density of the system are continuously monitored to ensure the convergence of the simulation. Additionally, the root mean square deviation (RMSD) is employed to analyze and verify whether the structural system has reached equilibrium (Zhong et al., 2024). The calculation formula for RMSD is provided in Eq. (1) (Pitera, 2014). Finally, under periodic boundary conditions, the model's rationality is assessed through density and PDF calculations.

$$RMSD(t) = \sqrt{\frac{\sum_{i}^{N} (r_i(t) - r_i(0))^2}{N}} \quad (1)$$

where N, $r_i(t)$ and $r_i(0)$ represent the number of particles, the position of the i atom at time and the initial position of the i atom, respectively.

2.3.2. ReaxFF MD simulation details

For this study, two shale kerogen samples, AY1-6 and AY2, are selected to construct the ReaxFF models. Their elemental compositions are similar, and they contain the same types of functional groups, but they differ markedly in their degree of aromatic condensation. This design is well suited to investigating how variations in aromatic condensation affect kerogen pyrolysis, in line with the objectives of this work. To isolate the influence of kerogen structure on the thermal cracking reactions, kerogen is treated as organic matter independent of inorganic mineral components. Accordingly, the models include only kerogen structures and neglect the effects of minerals on the reaction pathways (Chen et al., 2025a, 2025b).

The choice of force field in the simulation system depends on the atoms involved. This study involves elements C, H, O, N, S. Therefore, C/H/O/N/S/B force field parameters are selected for pyrolysis simulation calculation of kerogen. This reaction force field is first employed by Castro-Markano et al. to examine the complex chemical processes in coal pyrolysis and coal char combustion (Castro-Marcano et al., 2012). Subsequent studies on kerogen-related pyrolysis mechanisms demonstrate the applicability of this force field (Zhao et al., 2022). In ReaxFF, the relationship between the total energy, potential energy and kinetic energy is shown in Eq. (2):

$$E_{\text{total}} = E_{\text{potential}} + E_{\text{kinetic}} \quad (2)$$

The system energy currently used by ReaxFF can be described by Eq. (3) (Sun et al., 2025):

$$E_{\text{potential}} = E_{\text{bond}} + E_{\text{over}} + E_{\text{under}} + E_{\text{val}} + E_{\text{pen}} + E_{\text{tors}} + E_{\text{conj}} + E_{\text{vdWaals}} + E_{\text{Coulomb}} \quad (3)$$

where E_{bond}, E_{over}, E_{under}, E_{val}, E_{pen}, E_{tors}, E_{conj}, E_{vdWaals}, and E_{Coulomb} represent the bond energy, overcoordination term, undercoordination term, valence angle term, penalty energy term, torsion angle term, conjugation term, van der Waals interactions, and Coulomb interactions, respectively.

Before the pyrolysis simulation of kerogen, the energy of the constructed kerogen cell is minimized using the conjugate gradient method. Subsequently, a 50 ps relaxation simulation is performed under the NVT ensemble at 200 K. The system's equilibrium is confirmed through RMSD analysis. The equilibrated configuration following relaxation is used as the initial structure for the subsequent pyrolysis simulation.

The combination of pyrolysis temperature of 2200 K and heating rate of 50 K/ps has achieved good results in the study of steam pyrolysis of oil shale kerogen (Zhao et al., 2022). In this study, the same temperature control conditions (2200 K, 50 K/ps) are applied. In the real system, periodic boundary conditions are applied. The atom type is set to full, and temperature control is managed using the Berendsen thermostat with a damping constant of 25 fs. The time step is set to 0.25 fs. In the NVT ensemble, the system temperature is first increased from 200 to 2200 K at a heating rate of 50 K/ps. After reaching 2200 K, pyrolysis simulations are performed for a duration of 340 ps at this temperature. Product fragments are identified by applying a bond-order cutoff of 0.3. Additionally, all ReaxFF MD simulations in this study are conducted on the LAMMPS platform.

3. Results and discussion

3.1. Analysis of the kerogen chemical structure

3.1.1. FTIR analysis

The FTIR spectra of shale kerogen from the Longmaxi Formation and their fitting curves in the wavenumber range of 1800–700 cm^{-1} are shown in Fig. 2, respectively. The infrared absorption spectra of AY1-6 and AY2 show a high degree of similarity. The difference is that the absorption peak intensity of AY1-6 is relatively high, which indicates that the maturity of AY2 kerogen may be relatively higher than that of AY1-6. As thermal maturity increases, oxygen-containing groups detach from the organic matter framework, aliphatic chains shorten, and the aromatic ring condensation becomes the main evolutionary path, and the intensity of the corresponding infrared absorption peaks changes accordingly (Huang et al., 2017; Painter et al., 1981).

The two main peaks of AY1-6 and AY2, located near 1633 and 3400 cm^{-1}, are attributed to aromatic carbon and hydroxyl groups, respectively. The peak in the wavenumber range of 3600–3400 cm^{-1} indicates the presence of moisture in the separated kerogen samples (Liu et al., 2021). The weak absorption peaks in the ranges of 1450–1370 cm^{-1} and 3000–2800 cm^{-1} suggest that oxygen-containing functional groups and long-chain aliphatic hydrocarbons in the kerogen samples significantly decrease under high-temperature pyrolysis. The peak around 1633 cm^{-1} is distinct and sharp, further confirming the presence of significant aromatic carbon in the chemical structure of the kerogen. The peak in the range of 900–700 cm^{-1} is assigned to the out-of-plane bending of aromatic C–H bonds. The peak at 750 cm^{-1} in both AY1-6 and AY2 exhibits the highest intensity in this region, indicating that disubstituted benzene rings are dominant.

Overall, most mineral absorption peaks in the kerogen spectrum disappear, indicating that the acid treatment has removed the majority of minerals from the shale. However, the absorption peak of pyrite at 421 cm^{-1} remains visible, as pyrite cannot be removed by HCl/HF acid treatment. It typically remains as the main residual mineral, and generally does not affect the study of the kerogen structure (Wang et al., 2022b).

3.1.2. XPS analysis

The correct distribution of heteroatom structures is essential for predicting reactivity and physical properties (Kelemen et al., 2007). XPS determines the distribution of heteroatoms in shale

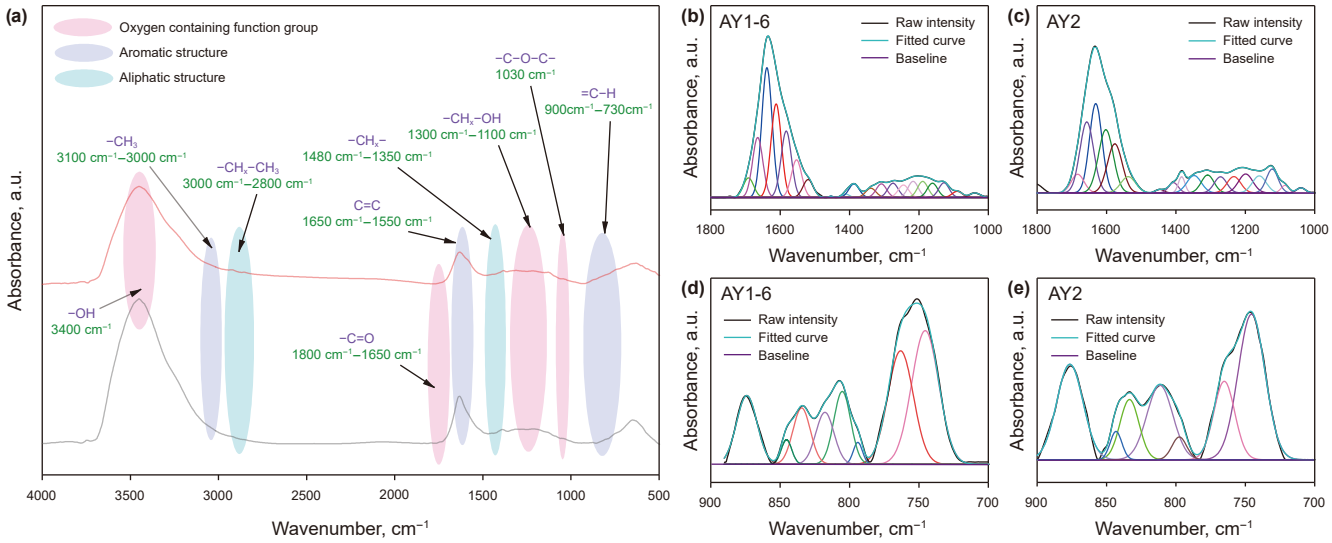

Fig. 2. Comparison of infrared spectra of AY1-6 and AY2 kerogen samples. **(a)** The FTIR spectrum of AY1-6 and AY2 kerogens, **(b)** the 1800–1000 cm^{-1} band of AY1-6, **(c)** the 1800–1000 cm^{-1} band of AY2, **(d)** the 900–700 cm^{-1} band of AY1-6, **(e)** the 900–700 cm^{-1} band of AY2.

kerogen and provides information on the relative content of different atomic types.

Consistent with the elemental test results (Table 1), AY1-6 and AY2 kerogen samples show quite similar elemental composition (Table 2). Carbon (C) is the dominant element in the kerogen structure, with an areal concentration exceeding 90%, which is significantly higher than that of nitrogen (N) and sulfur (S). The areal concentration ratio of N to S is approximately 3:2, indicating that nitrogen content in the samples is higher than sulfur content.

Based on the XPS fitting results (Fig. 3), the oxygen in the AY1-6 and AY2 samples predominantly exists in three forms: C=O double bonds, C–O single bonds, and carboxyl group O–C=O. Among these, C–O accounts for about 68% of the total oxygen content, which is significantly higher than that of C=O and O–C=O. This suggests that AY1-6 and AY2 are rich in hydroxyl or ether groups, followed by carbonyl, and carboxylic acids. Nitrogen is primarily present as pyrrole, with a relative content of about 50%, followed by pyridine and quaternary nitrogen forms. The sulfur fitting results (Fig. 3(c) and (f)) show three pairs of peaks corresponding to sulfurether sulfur, thiophene sulfur, and sulfoxide sulfur. Sulfoxide sulfur is the predominant form, accounting for more than half of the total sulfur atoms. Based on the above analysis, it can be concluded that the heteroatom oxygen in the kerogen is mainly in the form of C–O single bonds, with pyrrole nitrogen and sulfoxide sulfur as the predominant forms of nitrogen and sulfur, respectively. The binding energy positions, distributions, and relative area percentages of the corresponding heteroatom functional groups are summarized in Table 3.

Table 2
The relative contents of different atoms of the AY1-6 and AY2 kerogen obtained from XPS spectra.

Name	Atomic fraction, %	
	AY1-6	AY2
C	94.81	95.14
N	3.20	3.11
S	2.00	1.75

3.1.3. ^{13}C NMR analysis

^{13}C NMR is primarily used to analyze the framework of organic matter. The spectrum can be divided into three regions: 0–90 ppm for aliphatic carbon peaks, 90–165 ppm for aromatic carbon peaks, and 165–220 ppm for carbonyl carbon peaks. The spectra of AY1-6 and AY2 are similar, primarily consisting of aromatic and aliphatic groups, with a small amount of carbonyl groups (Fig. 4(a)). The intensity of the aromatic carbon peaks is significantly greater than that of the aliphatic carbon peaks, indicating that aromatic carbon is the dominant component in the kerogen structure. Aliphatic and carbonyl carbons serve to connect the aromatic structural units or exist as short branches. Additionally, the carboxyl carbon content in AY1-6 and AY2 is lower than that of the carbonyl carbon, indicating that the C=O double bond primarily exists as a carbonyl functional group. This is consistent with the XPS C1s peak analysis results. The residual curve of the nuclear magnetic fitting spectrum (Fig. 4(b) and (c)) and the experimental spectrum fluctuates slightly, indicating that the peak separation method is appropriate. By integrating the different chemical shifts, 12 structural parameters of the carbon backbone are obtained (Table 4).

According to the NMR fitting results (Table 4), in the macromolecular structure of the AY1-6 and AY2 kerogen, the aromatic carbon mainly exists as protonated aromatic carbon. The alkyl-substituted carbons (side-chain aromatic carbons) in AY1-6 and AY2 account for 5.28% and 7.08% of the total carbon signal, respectively, while the bridged aromatic carbons represent 11.23% and 20.22% of the total carbon signal, respectively. This suggests that, compared to alkyl functional groups, the aromatic structural units in AY1-6 and AY2 kerogen are mainly connected through aryl substituent groups. The length of the aliphatic carbon chain (C_n) is determined by the ratio of the NMR fractions of aliphatic carbons ($f_{al}^{B} + f_{al}^{H}$) to the aromatic carbon side chain fraction (f_{ar}^{C}). The C_n values close to 1.0 (Table 5) suggest that almost all aliphatic carbons are in the form of methyl groups (Kelemen et al., 2007). The aromatic cluster size (X_{BP}) reflects the ratio of aromatic bridge carbon to total aromatic carbon, which is used to determine the condensation degree of aromatic hydrocarbons. The X_{BP} of AY1-6 is 0.15, while the X_{BP} of AY2 is 0.31. The degree of substitution (D) of the aromatic ring reflects the content of carbon in the aromatic carbon bonded with non-hydrogen atoms. The D of kerogen AY1-6 and AY2 are 38% and 45%, respectively, indicating that the average

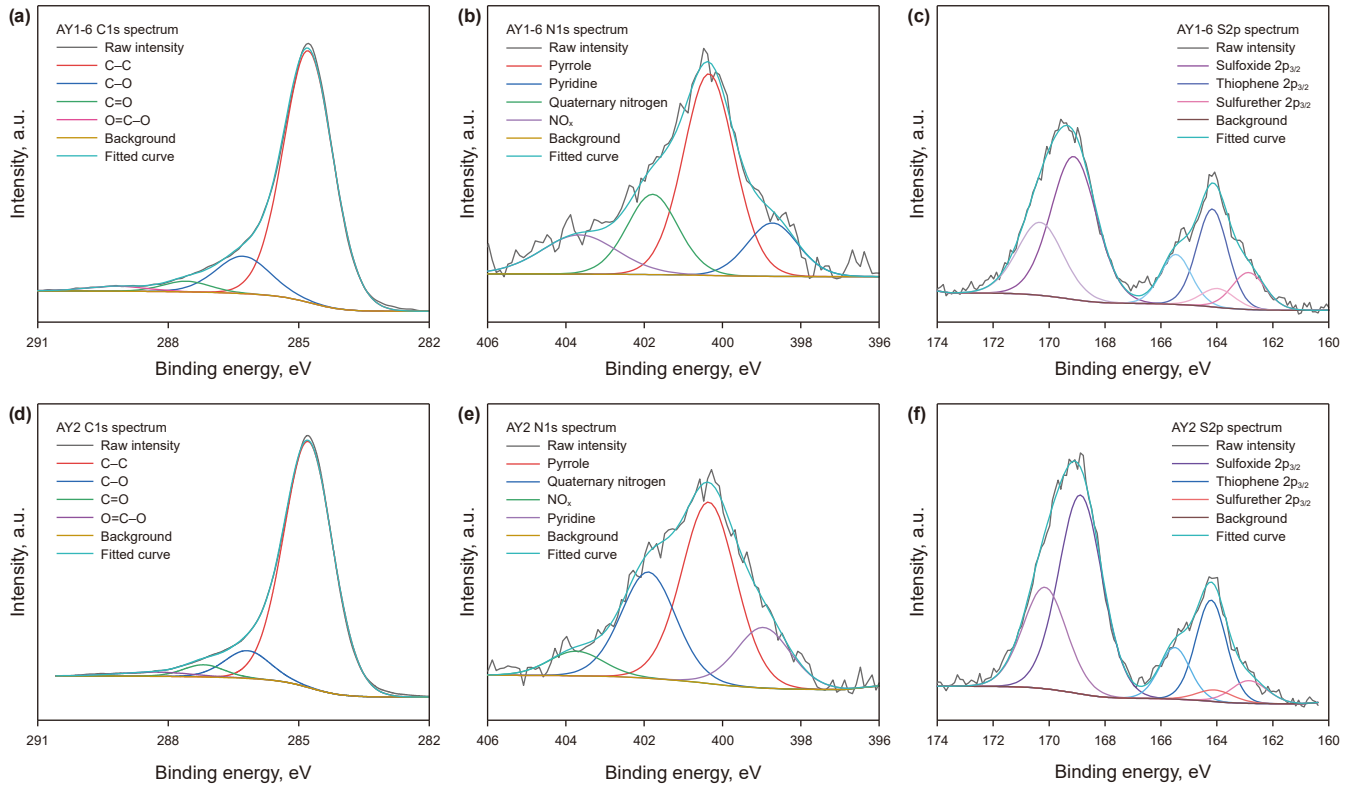

Fig. 3. The experimental and fitted XPS spectra of AY1-6 and AY2 kerogen samples: **(a)**, **(b)**, **(c)** C1s, N1s and S2p scans of AY1-6, respectively; **(d)**, **(e)**, **(f)** C1s, N1s and S2p scans of AY2, respectively.

Table 3
Distribution of heteroatom functional groups in AY1-6 and AY2 obtained from XPS spectra.

Name	Functional group	AY1-6		AY2	
		Binding energy, eV	Relative content, %	Binding energy, eV	Relative content, %
C1s	C–C, C–H	284.80	78.20	284.80	85.36
	C–O, C–OH	286.30	10.78	286.18	8.96
	C=O	287.50	3.71	287.18	3.55
	O–C=O	290.20	1.23	288.28	2.13
N1s	Pyridine	398.72	13.55	398.96	16.23
	Pyrrole	400.35	51.22	400.35	48.63
	Quaternary nitrogen	401.78	20.41	401.89	28.51
	Nitrogen oxide	403.65	14.83	403.73	6.62
S2p	Sulfurether $2p_{3/2}$	162.87	11.40	162.85	6.47
	Sulfurether $2p_{1/2}$	163.97		164.07	
	Thiophene $2p_{3/2}$	164.16	28.11	164.21	24.60
	Thiophene $2p_{1/2}$	165.46		165.51	
	Sulfoxide $2p_{3/2}$	169.12	60.49	168.88	68.93

substituted aromatic carbon atoms in the aromatic ring are 2 and 4, respectively.

In summary, the difference between the carbon skeletons of AY1-6 and AY2 lies primarily in their degree of aromatic condensation (X_{BP}). The higher degree of aromatic condensation in AY2 provides it with better thermal stability and a higher pyrolysis activation energy (Cypres, 1987). However, this compact structure may limit the accessibility of active sites. Additionally, the dominant non-polar C/C and C/H bonds in the aromatic rings exhibit a weak affinity for water molecules, leading to significant hydrophobicity in AY2. In contrast, AY1-6 exhibits stronger hydrophilicity due to its structural differences (Jagadisan and Heidari, 2019), which may lead to different product distributions during hydrous pyrolysis.

3.1.4. Reconstruction and validation of the kerogen

In the carbon skeleton, the aromatic cluster structure is designed according to the X_{BP} value. Most non-aromatic carbons are long straight or branched chains (Ungerer et al., 2015). To achieve a better match with the H/C ratio, some saturated rings are introduced to make the structure more compact. Heteroatoms, such as O, N, and S, are incorporated into the molecular model as basic structures or functional groups during its construction. Sulfur-containing substances identified through experimental analysis mainly include sulfurether, thiophene, and sulfoxides. Nitrogen-containing substances primarily consist of pyrrole, pyridine, and quaternary nitrogen. Oxygen-containing substances are mainly considered to include ether bonds, hydroxyl groups, carbonyl groups, and carboxyl groups. Given the influence of

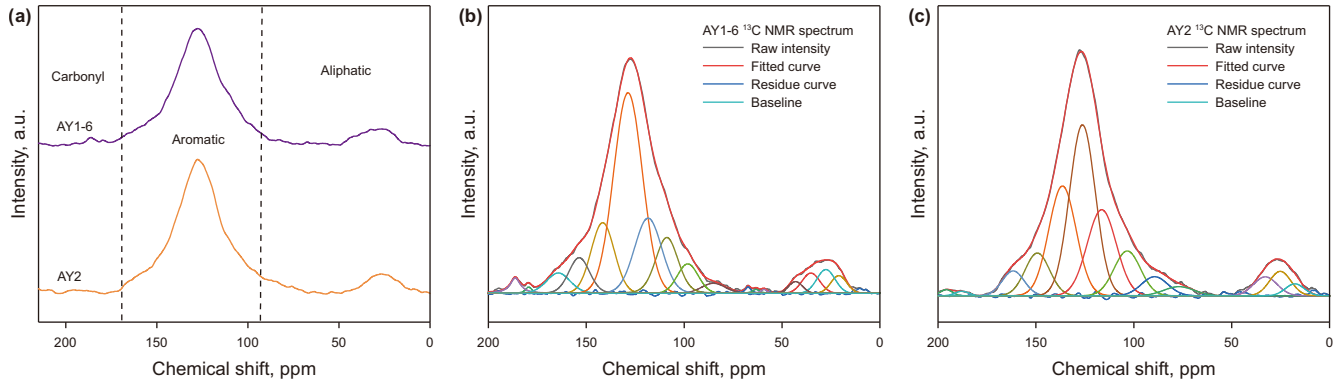

Fig. 4. The experimental **(a)** and fitted ^{13}C NMR spectra of AY1-6 **(b)** and AY2 **(c)**.

Table 4
The carbon skeleton parameters of kerogen AY1-6 and AY2 derived from the fitting data of ^{13}C NMR experimental spectra.

Symbol	Carbon type	Chemical shift, ppm	Molar content, %	
			AY1-6	AY2
f_{al}^{M}	Aliphatic methyl	17	–	1.52
f_{al}^{A}	Aromatic methyl	20	1.92	–
f_{al}^{B}	Aliphatic C (2) carbon	25, 27	2.94	3.53
f_{al}^{H}	Methylene	32, 35	2.47	3.01
f_{al}^{D}	Methine, quaternary sp^3 carbon	43	1.12	–
f_{al}^{O}	Oxygen-methylene	59	0.23	–
	Oxygen-methine	63, 67	0.64	1.86
	Oxygen-aliphatic ring	85, 89	1.64	3.40
f_{ar}^{A}	Oxygen-aromatic ring	98–108	13.33	8.01
f_{ar}^{H}	Protonated aromatic carbon	116–128	53.68	46.76
f_{ar}^{B}	Bridged aromatic carbon	136, 141	11.23	20.22
f_{ar}^{C}	Branched aromatic carbon	149, 153	5.28	7.08
f_{ar}^{O}	Oxygen-aromatic carbon	161, 164	3.54	3.68
f_{a}^{O}	Carboxyl, carbonyl	180–200	1.97	0.93

Table 5
The lattice parameters of kerogen AY1-6 and AY2 derived from the fitting data of ^{13}C NMR experimental spectra.

Symbol	Lattice parameters	Definition	Value	
			AY1-6	AY2
f_{al}	Aliphaticity	$f_{al}^{M}+f_{al}^{A}+f_{al}^{B}+f_{al}^{H}+f_{al}^{D}+f_{al}^{O}$	10.96	13.32
f_{ar}	Aromaticity	$f_{ar}^{A}+f_{ar}^{H}+f_{ar}^{B}+f_{ar}^{C}+f_{ar}^{O}$	87.06	85.75
X_{BP}	Degree of condensation	$f_{ar}^{B}/(f_{ar}^{A}+f_{ar}^{H}+f_{ar}^{C}+f_{ar}^{O})$	0.15	0.31
BI	Aliphatic branch	$(f_{al}^{D}+C^{*}H\text{-}O)/f_{al}$	0.16	0.14
D	Aromatic substitution	$1-f_{ar}^{H}/f_{ar}$	0.38	0.45
C_n	Aliphatic chain length	$(f_{al}^{B}+f_{al}^{H})/f_{ar}^{C}$	1.04	0.92

moisture in the sample, we focus mainly on ether bonds during the modeling process.

After analyzing the fragments of the kerogen structure, the crosslinking of these species is key to constructing the 2D kerogen model, as the chemical shifts of carbon atoms connected to different species vary. By continuously adjusting the aromatic skeleton, aliphatic chain length, and heteroatom distribution, the predicted NMR spectra are in good agreement with the experimental ^{13}C NMR data (Fig. 5(a) and (b)). The molecular formulas for the organic matter in AY1-6 and AY2 shale are ultimately determined to be $C_{233}H_{114}O_{18}N_7S_4$ (molecular weight 3424 g/mol) and $C_{237}H_{120}O_{16}N_7S_4$ (molecular weight 3446 g/mol), respectively. The optimized 3D molecular structures of AY1-6 and AY2 are shown in Fig. 5(c) and (d). The specific details of the molecular model for Guizhou Longmaxi are shown in Table 6. The molecular structural characteristics of AY1-6 and AY2 are well represented in the simulations, and the models effectively preserve their aromatic condensation features.

Building upon the 2D kerogen structures, we constructed the 3D kerogen cells following the steps outlined in Section 2.3.1. Fig. 6 shows the 3D structures of the kerogen unit cells. The sizes of the AY1-6 models range from 3.69 × 3.69 × 3.69 nm^3 to 3.84 × 3.84 × 3.84 nm^3, with the number of atoms varying between 3750 and 4050. The sizes of the AY2 models range from 3.67 × 3.67 × 3.67 nm^3 to 3.83 × 3.83 × 3.83 nm^3, with the number of atoms ranging from 3840 to 4143. The optimized densities of the kerogen unit cells obtained in this study (1.1–1.2 g/cm^3) are similar to the previously recorded density data for kerogen (1.1–1.4 g/cm^3) (Atmani et al., 2017; Okiongbo et al., 2005), which to some extent reflects the physical structural characteristics of the kerogen structure. Finally, the established 3D hydrous kerogen cells are shown in Fig. 6(a) and (c). To verify the reliability of the kerogen modeling system, we conducted a carbon atom PDF analysis on the 3D kerogen models of the AY1-6 and AY2. The total PDF, $g(r)$, of the system is composed of both intermolecular and intramolecular interactions. Since the contribution of intermolecular interactions to the total $g(r)$ is negligible in the short-range, the first three characteristic peaks in the function mainly reflect the distance information between atom pairs within the same polyaromatic layer (Castro-Marcano et al., 2012).

As shown in Fig. 6, the first characteristic peak for both the AY1-6 and AY2 models appears at approximately 1.40 Å, which correlates well with the composition ratio of carbon bond types observed in the experiment. For the AY1-6 sample, the weighted calculation result for aromatic carbon (87.06%) and aliphatic carbon (10.96%)

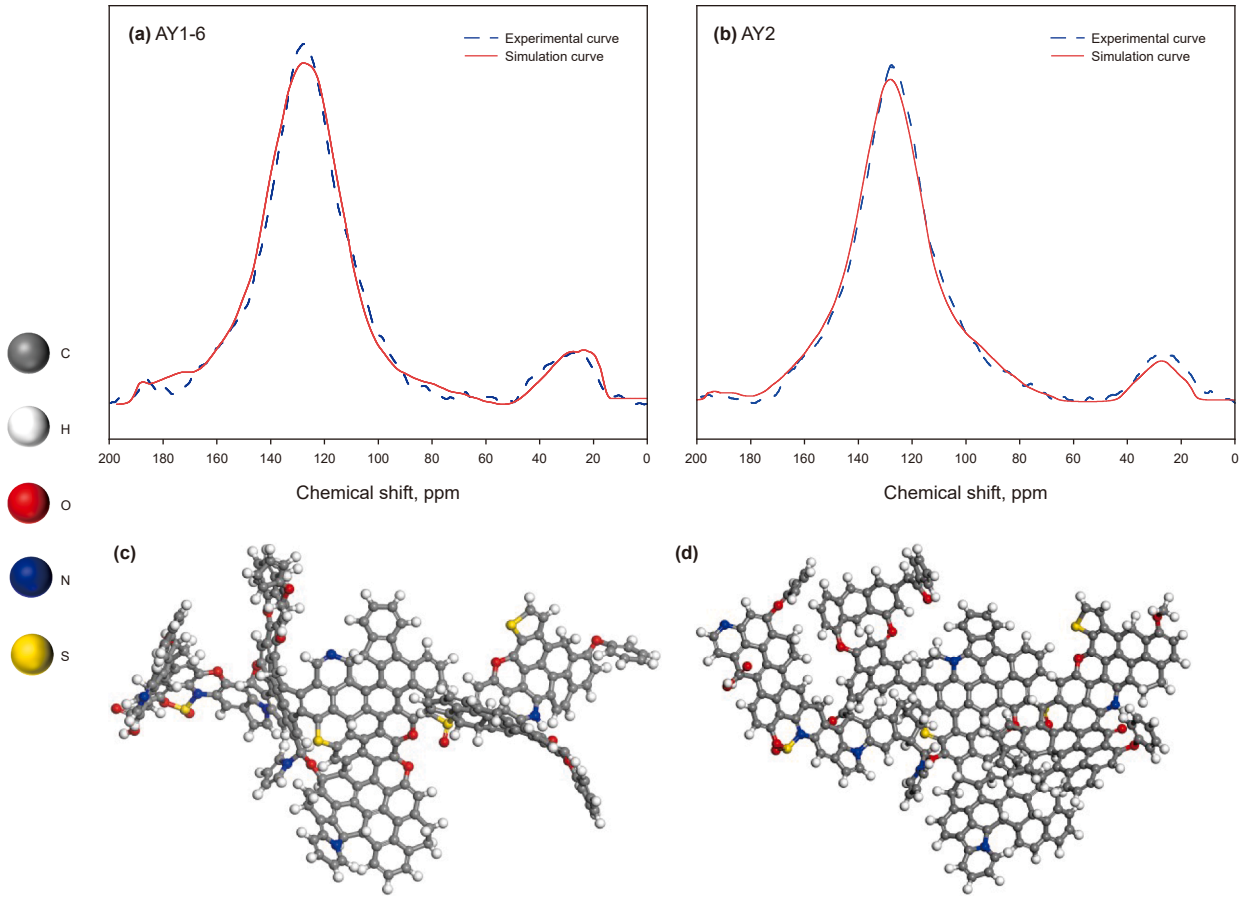

Fig. 5. Predicted and experimental ^{13}C NMR spectra of kerogen AY1-6 **(a)** and AY2 **(b)**, and comparison of the optimized molecular structures of AY1-6 **(c)** and AY2 **(d)**.

Table 6
The structural parameters and functional group distribution of AY1-6 and AY2 kerogen molecular models.

Property	Structural parameter	AY1-6		AY2	
		Experimental	Modeling	Experimental	Modeling
Atomic compositions	H/C	0.43	0.49	0.43	0.51
	O/C	0.05	0.07	0.04	0.07
	N/C	0.03	0.03	0.03	0.03
	S/C	0.02	0.017	0.02	0.02
C groups	f_{ar}	87.06	78.96	85.75	85.65
	f_{al}	10.96	20.17	13.32	12.66
	X_{BP}	0.15	0.16	0.31	0.33
	C_n	1.02	0.24	0.92	0.37
	BI	0.16	0.19	0.16	0.17
	D	0.38	0.66	0.48	0.70
O groups	C–O (mol% of C–O)	71.64	87.50	61.2	71.00
	Carbonyl (>C=O) (mol% of C–O)	17.84	6.25	24.24	21.00
	Carboxyl (–COOH) (mol% of C –O)	10.52	6.25	14.55	7.00
N groups	Pyrrole (mol% of N)	60.13	42.85	52.01	42.00
	Pyridine (mol% of N)	15.91	14.28	17.38	14.00
	Quaternary nitrogen (mol% of N)	23.96	42.85	30.53	42.00
	NO_x (mol% of N)	14.83	0.00	0.00	0.00
S groups	Thiophene (mol% of organic S)	28.11	25.00	24.60	25.00
	Sulfoxide (mol% of organic S)	60.48	50.00	68.93	50.00
	Sulfurether (mol% of organic S)	11.40	25.00	6.47	25.00

content is 1.38 Å (Formula: 1.39 Å × 0.8706 + 1.54 Å × 0.1096, where 1.39 Å represents the aromatic C–C bond and 1.54 Å represents the alkyl C–C bond (Castro-Marcano et al., 2012)). The experimental weighted calculation result for the AY2 sample is 1.39 Å (Formula: 1.39 Å × 0.8575 + 1.54 Å × 0.1332). The composition ratio of the carbon bond types in the two models is close to the measured value. This correspondence confirms the reasonable ratio of sp^2 (aromatic C–C bond) to sp^3 (alkyl C–C bond) hybrid carbon in the models. The

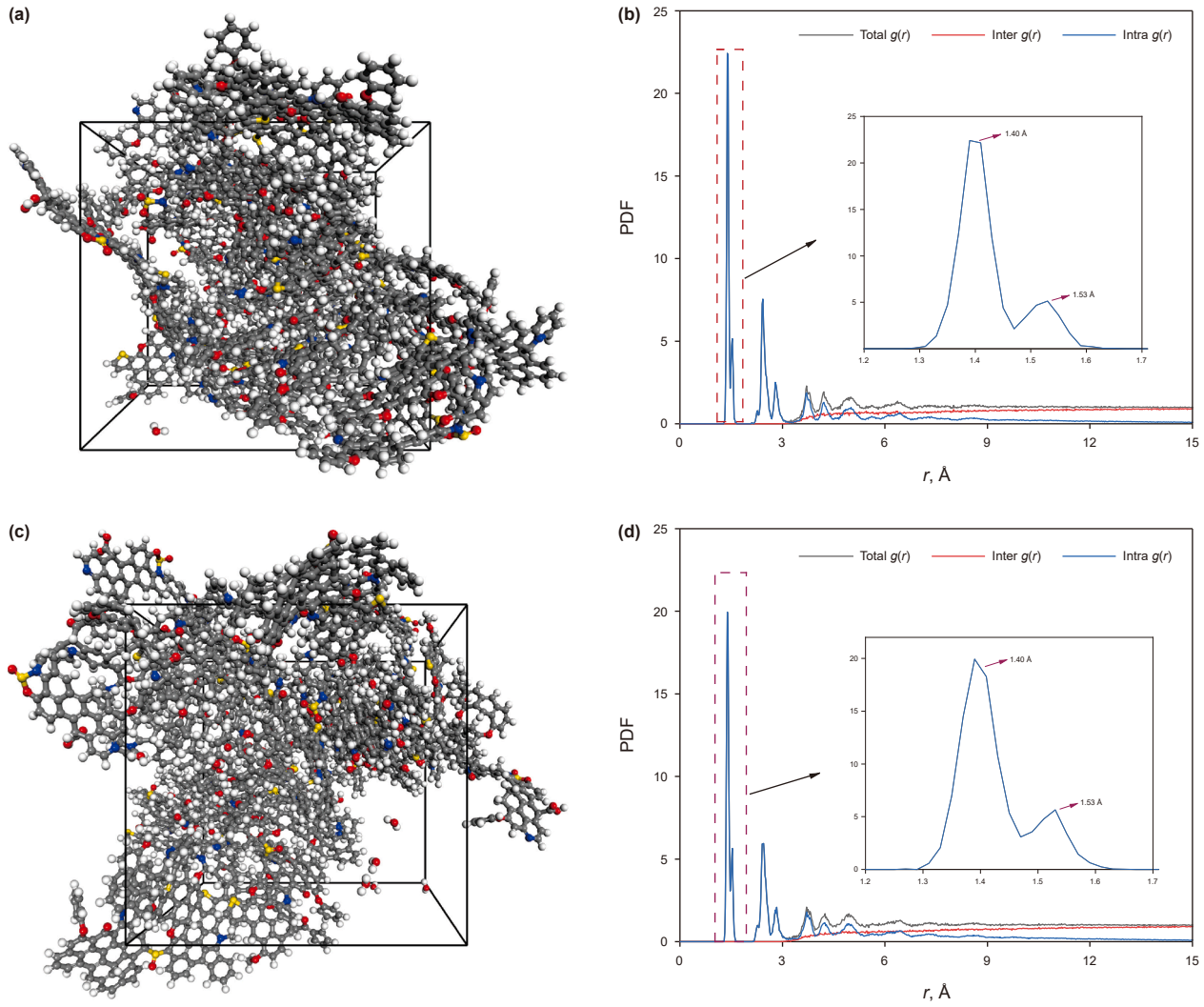

Fig. 6. 3D models of AY1-6 kerogen **(a)** with a moisture content of 0.5 wt.% and AY2 kerogen **(c)** with a moisture content of 1 wt.%, along with their corresponding C–C pairwise distribution functions $g(r)$ ((**b**) AY1-6, (**d**) AY2). The total $g(r)$ function is the sum of intermolecular (inter $g(r)$) and intramolecular (intra $g(r)$) contributions.

second characteristic peak appears near 1.53 Å, which can be attributed to the superposition effect of aliphatic carbon-aliphatic carbon bond (1.54 Å) and aliphatic-aromatic single carbon bond (about 1.50 Å).

3.2. Pyrolysis simulation in ReaxFF

The shale of Longmaxi Formation is currently in the gas generation stage, and the industrial exploitation is mainly based on shale gas. Therefore, this study primarily focuses on the variation trends of gaseous hydrocarbons. According to the number of C atoms, C_1–C_4 fragments are considered as organic gas, while C_{40+} fragments are considered as kerogen or char (Chen et al., 2023; He et al., 2023; Zhang et al., 2019b). In addition, we investigated the evolution of carbon-free products, with particular emphasis on carbon-free free radicals (hereinafter referred to as inorganic products and inorganic free radicals), under different conditions.

In this study, the system has reached a stable state before formal pyrolysis began. The RMSD change curves (Fig. 7(a) and (b)) show that the system's RMSD value initially increases from 0 Å to approximately 10 Å, indicating the presence of stress concentration points before structural relaxation. After 20 ps, there is no significant change, suggesting that the atoms no longer undergo substantial spatial movement, and the system has reached equilibrium. The temperature control curve (Fig. 7(c)) largely matches the expected settings. The first 50 ps correspond to the heating phase, during which the temperature gradient remains stable at the set value. In the subsequent isothermal phase (>50 ps), temperature fluctuations remain within a controllable range.

The energy variation during the simulation is presented in Fig. 8. During the initial heating stage (0–50 ps), the total energy and potential energy curves for the AY1-6 and AY2 systems increase in parallel at similar rates. This is because the increase in temperature raises the system's kinetic energy, causing the intermolecular distance to increase and the potential energy to decrease. After the temperature is raised, the total energy of the system reaches a stable plateau (Guo et al., 2024; Yang et al., 2025a). The system's total energy and potential energy are positively correlated with the moisture content. This is because water has a high specific heat capacity, and its evaporation absorbs substantial heat, causing the system to absorb more energy during heating. This suggests that, in the shale hydrocarbon generation process, hydrous systems require more energy to reach the pyrolysis temperature. This may delay the pyrolysis time (Hu et al.,

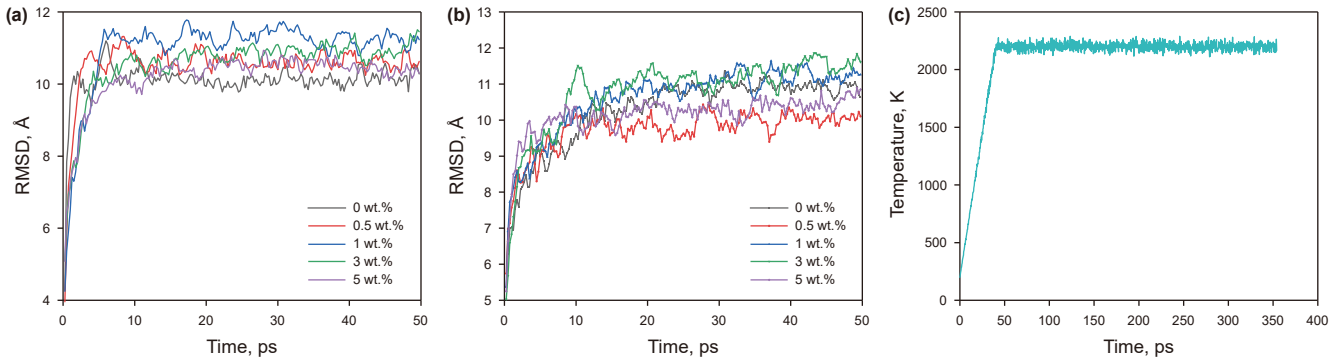

Fig. 7. The RMSD of AY1-6 **(a)** and AY2 **(b)** during relaxation and the temperature control process **(c)** during the pyrolysis curve in the ReaxFF.

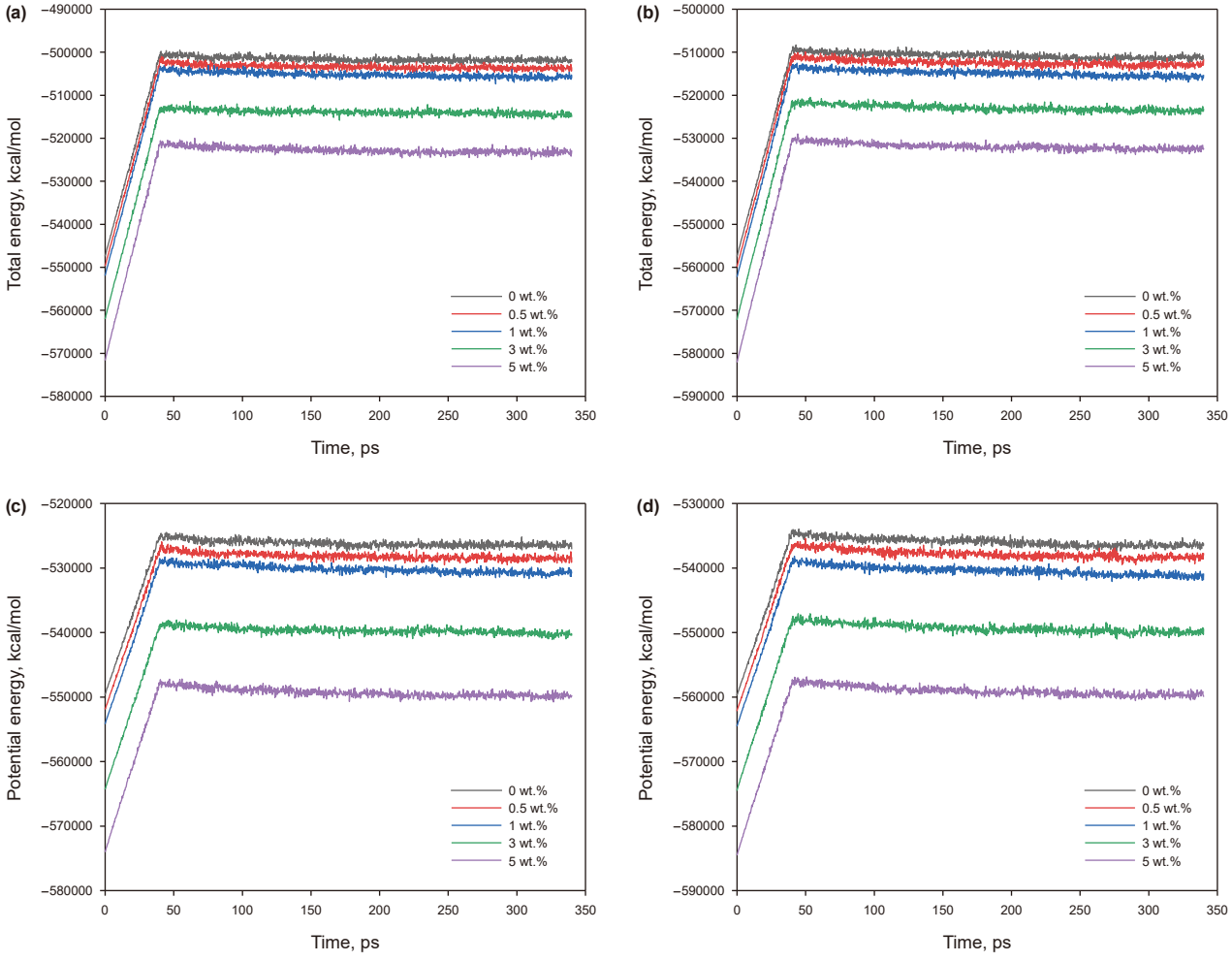

Fig. 8. The total energy and potential energy curves of AY1-6 and AY2 under different moisture contents in pyrolysis simulation: **(a)** and **(c)** are the total energy and potential energy of the AY1-6 system, respectively; **(b)** and **(d)** are the total energy and potential energy of the AY2 system, respectively.

2017). Furthermore, the total energy and potential energy of the AY2 system are slightly higher than those of the AY1-6 system. This shows that the kerogen molecules with high structural stability need higher energy to heat up to the same target temperature, and it is more difficult to react under the same conditions.

Using VMD software, the evolution of the system's configuration at different time points during the pyrolysis simulation of AY1-6 with a moisture content of 1 wt.% is visualized (Fig. 9). Comparing the configurations at the four time points, it is observed that with an increase in temperature, atomic motion accelerates, filling the voids in the simulation box and increasing the probability of intermolecular collisions. Meanwhile, the six-membered rings gradually open, and free radicals are continually released. As pyrolysis progresses, the number of free radicals increases. These free radicals attack polyaromatic hydrocarbon sheets and other molecular fragments, triggering condensation between atoms and molecules, leading to the formation of smaller cyclic and linear structures.

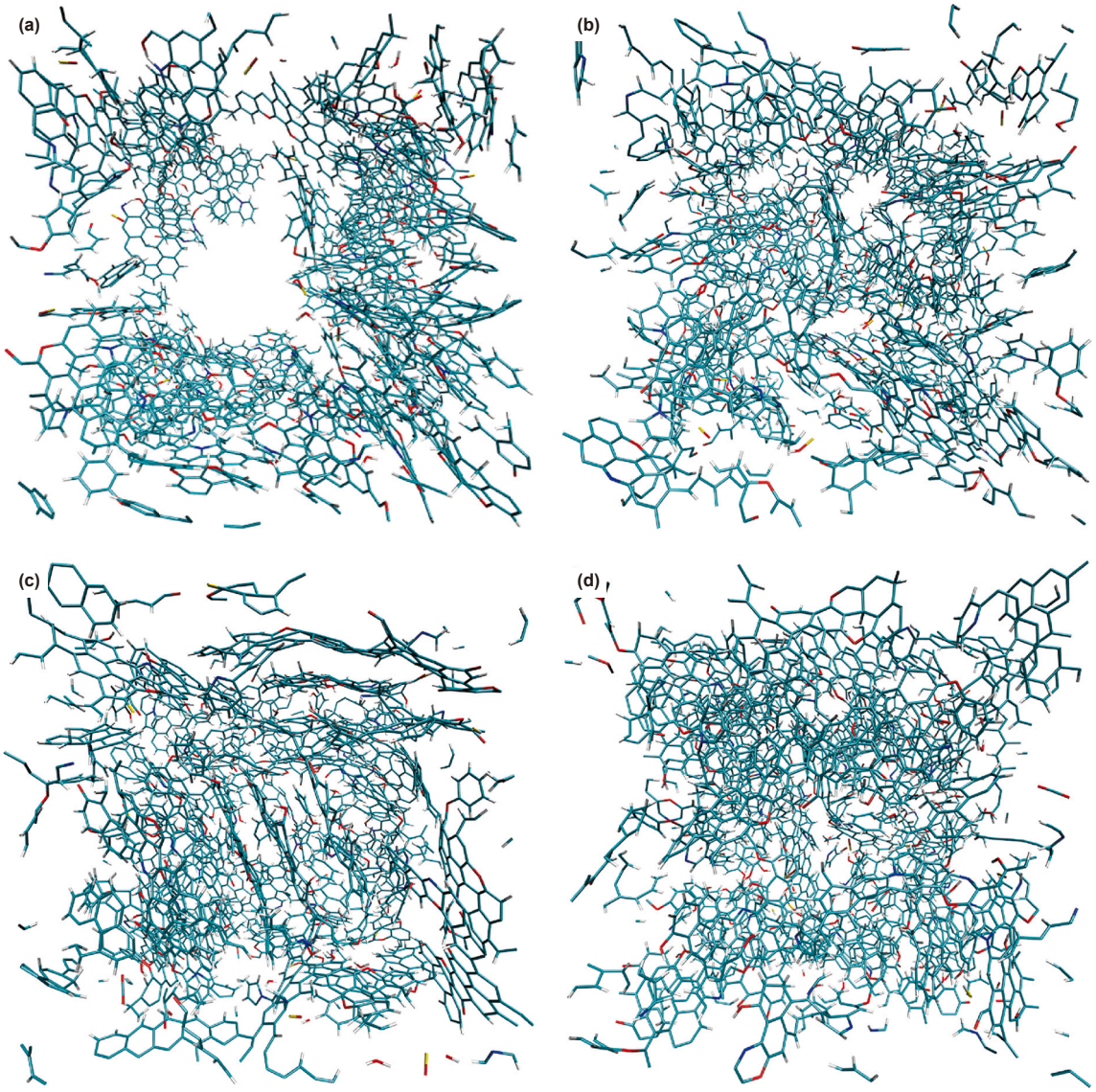

Fig. 9. The evolution of the system configuration of AY1-6 kerogen with 1 wt.% moisture content at different stages of pyrolysis simulation. **(a)** Initial configuration, **(b)** intermediate configuration at 40 ps, **(c)** intermediate configuration at 200 ps, **(d)** final configuration at 300 ps, respectively.

3.2.1. Effect of moisture content on pyrolysis products

Figs. 10 and 11 illustrate the evolution characteristics of the pyrolysis products for AY1-6 and AY2 kerogen under different moisture content conditions, respectively. For AY1-6, the gaseous hydrocarbon yield increases rapidly in the initial stage (0–70 ps) (Fig. 10(a)), after which the rate of increase slows down. This trend is confirmed by the variation in the number of C atoms, as shown in Fig. 10(b). By analyzing the average gaseous hydrocarbon yield after 80 ps (Fig. 10(c)), it can be observed that as the moisture content increases from 0 to 0.5 wt.%, the gaseous hydrocarbon yield decreases. The yield reaches its peak when the moisture content is 1 wt.%. As the moisture content continues to rise, the gaseous hydrocarbon yield in the hydrous system remains higher than that of the anhydrous groups, but the promoting effect of water molecules becomes significantly weaker. The char yield (Fig. 10(d)) increases rapidly during the heating phase (0–50 ps), after which the rate of increase slows down and begins to decrease around 100 ps. The change in the number of C atoms in char (Fig. 10(e)) shows that a medium moisture content (1 and 3 wt.%) is most conducive to the pyrolysis of the carbon skeleton into smaller molecular products.

Compared to AY1-6, AY2 exhibits a higher gaseous hydrocarbon yield, although its growth rate is lower (Fig. 11(a)). The growth of gaseous hydrocarbons in both AY1-6 and AY2 can be divided into two phases: a rapid growth phase and a slow growth phase. In AY1-6, the rapid growth phase lasts for 70 ps, whereas in AY2, it extends to 130 ps. Within the hydrous groups, the gaseous hydrocarbon yield generally increases with increasing moisture content (Fig. 11(c)). The highest yield occurs at a moisture content of 5 wt.%, while, similar to the AY1-6 system, the yield is lowest at 0.5 wt.%. Regarding char evolution, the yield for each group increases sharply during the 0–50 ps heating stage. When the temperature stabilizes at 2200 K (>50 ps), char formation slows down and enters the decay phase at 150 ps (Fig. 11(d)). The significant decrease in the number of carbon atoms in the char (Fig. 11(e)), especially the substantial loss in the 5 wt.% moisture group, provides strong evidence that a high moisture content environment can effectively promote the cracking of AY2.

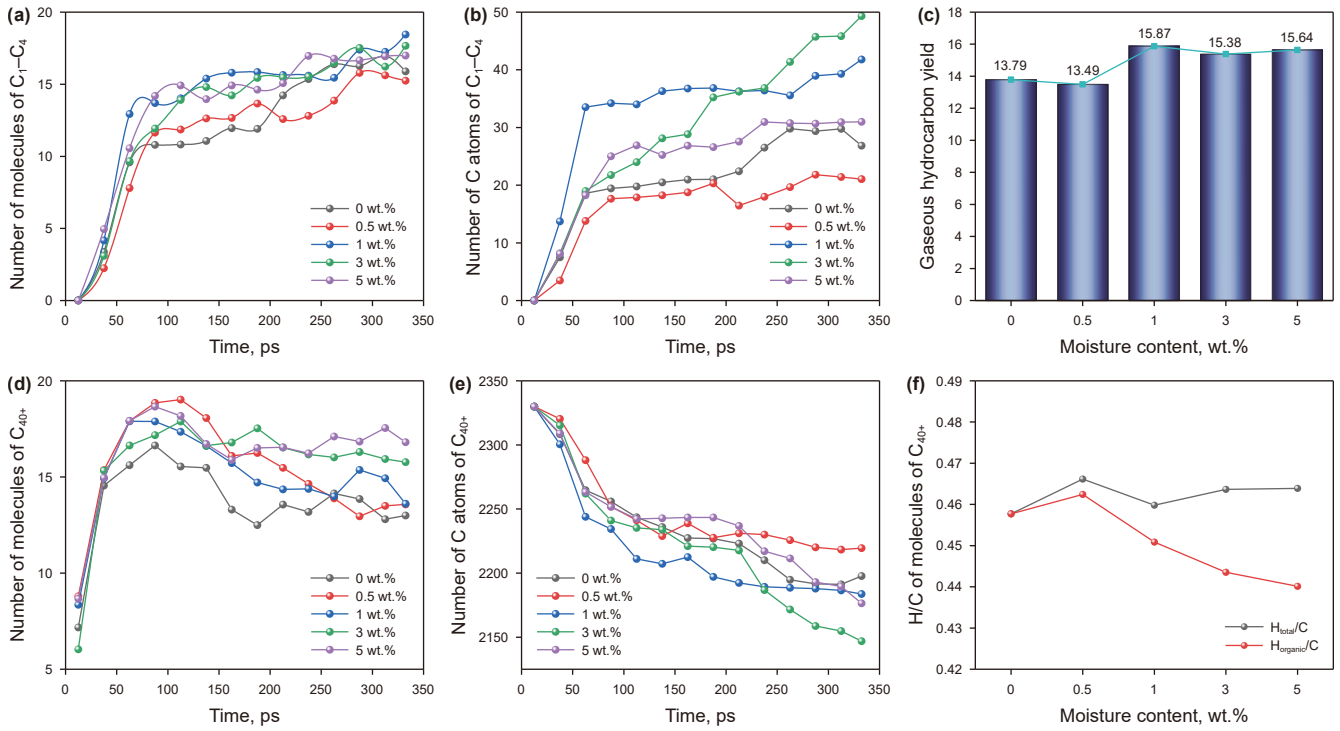

Fig. 10. Product evolution and characteristics of gaseous hydrocarbons and char in AY1-6 during pyrolysis, where (**a**) represents the yield of gaseous hydrocarbons (C_1–C_4), (**b**) represents the carbon number distribution of gaseous hydrocarbons (C_1–C_4), (**c**) the average yield of gaseous hydrocarbons (C_1–C_4) after 80 ps, (**d**) represents the yield of char (C_{40+}), (**e**) represents the carbon number distribution of char (C_{40+}), and (**f**) represents the hydrogen-to-carbon ratio (H/C) of char (C_{40+}).

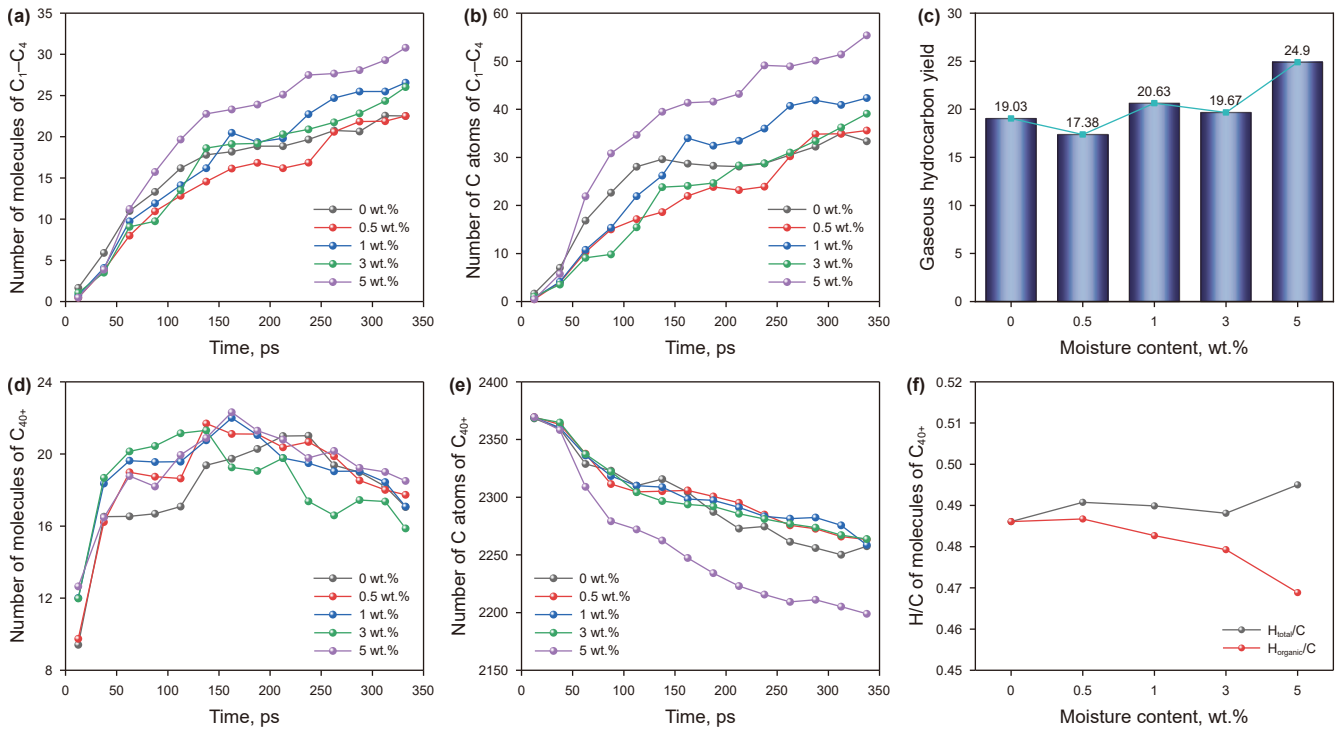

Fig. 11. Product evolution and characteristics of gaseous hydrocarbons and char in AY2 during pyrolysis, where (**a**) represents the yield of gaseous hydrocarbons (C_1–C_4), (**b**) represents the carbon number distribution of gaseous hydrocarbons (C_1–C_4), (**c**) the average yield of gaseous hydrocarbons (C_1–C_4) after 80 ps, (**d**) represents the yield of char (C_{40+}), (**e**) represents the carbon number distribution of char (C_{40+}), and (**f**) represents the hydrogen-to-carbon ratio (H/C) of char (C_{40+}).

The peak gaseous hydrocarbon yield in both systems occurs in the hydrous groups, suggesting that water facilitates the cracking of kerogen. This is further supported by the hydrogen-to-carbon ratio in the char products. The hydrogen (H) is categorized based on its source: hydrogen from kerogen ($H_{organic}$), hydrogen from water molecules (H_{water}), and hydrogen from both sources (H_{total}).

Using this distinction, two types of hydrogen-to-carbon ratios are calculated. According to Fig. 10(f) and 11(f), the total hydrogen-to-carbon ratio (H_{total}/C) of the system increases with the increase of moisture content. However, the hydrogen-to-carbon ratio of pure organic matter ($H_{organic}$/C) decreases. This contrast highlights two roles of H_2O in pyrolysis: on one hand, water promotes the cracking of kerogen, and as the moisture content increases, the hydrogen-to-carbon ratio of the organic matter decreases, indicating a deeper level of dehydrogenation. On the other hand, water molecules increase the saturation of the kerogen molecules by providing hydrogen, which leads to an increase in the overall hydrogen-to-carbon ratio. However, when the moisture content is too low, it may inhibit the pyrolysis of kerogen. For example, at a moisture content of 0.5 wt.%, the gaseous hydrocarbon yields of AY1-6 and AY2 are both lower than those of the anhydrous pyrolysis groups, whereas the maximum yields are achieved at 1 and 5 wt.%, respectively. This is verified by the hydrogen-to-carbon ratio of the char molecules: at the 0.5 wt.% moisture content, the hydrogen-to-carbon ratio of pure organic matter is higher than that of the anhydrous groups, suggesting that the presence of water molecules may inhibit the dehydrogenation reaction of kerogen. This may result from the fact that under low moisture content conditions, water does not provide enough ·H, but instead consumes the free radicals produced during kerogen cracking, such as by combining with ·H to form H_2. Therefore, this results in insufficient dehydrogenation (high H/C) and low gaseous hydrocarbon yield.

Regarding the pyrolysis rate, the gaseous hydrocarbons and heavy components of AY2 are significantly lower than those of AY1-6. This is likely due to AY2 ($X_{BP} = 0.30$) having a higher degree of aromatic condensation, where the dense structure formed by aromatic ring stacking hinders the penetration of water molecules into internal reaction sites, thus slowing down the reaction and prolonging its duration. The corresponding percentage of water molecules also verifies this. As shown in Fig. 12(a) and (b), within 0–70 ps, the percentage of water molecules in the AY1-6 hydrous groups decreases rapidly, whereas that in the AY2 hydrous groups decreases more slowly and continues to decrease until about 130 ps.

Although kerogen mainly consists of hydrophobic carbon skeletons, heteroatoms (such as O atoms, N atoms, and S atoms) increase the polarity of the molecular surface through polar functional groups (Lawal et al., 2020; Yang et al., 2025b), thereby improving the interaction between water and kerogen. This characteristic shifts the optimal moisture content threshold for promoting pyrolysis, primarily through hydrogen bonding (Sanchouli et al., 2024; Zhou et al., 2022). The primary variable in this study is the degree of aromatic condensation. In practical applications, slight structural differences exist between AY1-6 and AY2, primarily in the number of polar functional groups. These differences can influence the local polarity and the number of hydrogen bonding sites, potentially leading to subtle shifts in the optimal moisture content threshold for promoting pyrolysis. Understanding these hydrogen bonds (H Bonds) is crucial for comprehending the distinct behaviors of the two kerogen types when interacting with water molecules. According to the Luzar-Chandler geometric criterion (donor-acceptor distance <0.35 nm, angle <30°) (Luzar and Chandler, 1993), O atoms form the majority of hydrogen bonds, accounting for over 70% of the total. N atoms follow, while S atoms contribute minimally to hydrogen bond formation. This result suggests that polar heteroatoms such as O atoms and N atoms are the primary sites for preferential adsorption and interaction with water molecules. The heteroatom ratio of the AY1-6 model is slightly higher than that of AY2, which helps explain why the number of water-kerogen hydrogen bonds in AY1-6 is significantly greater than in AY2 under the same moisture content. However, further quantitative analysis revealed that, at a moisture content of 5 wt.%, the O atoms in the kerogen molecules of AY1-6 formed an average of 0.170 hydrogen bonds, while those in AY2 formed an average of 0.168 hydrogen bonds. This difference can be attributed to the more open spatial distribution of functional groups in AY1-6, which facilitates water interaction. In contrast, the high aromatic condensation in AY2 leads to a denser structure, impeding water penetration into the internal sites. Therefore, water molecules are more likely to form hydrogen bond networks on the surface of AY1-6, which in turn promotes the breaking of chemical bonds, such as C–O, and facilitates hydrogen transfer. This structural difference directly influences the optimal moisture content threshold for promoting pyrolysis: AY1-6 reaches the peak of gaseous hydrocarbons at a moisture content of 1 wt.%, whereas AY2 requires a moisture content of 5 wt.% to compensate for low-polarity sites and osmotic resistance. Under their respective optimal moisture content conditions, the AY2 model forms significantly more hydrogen bonds than the AY1-6 model (Fig. 12(c) and (d)). These results suggest that the aromatic condensation structure of the kerogen is the primary factor determining the optimal moisture content threshold. The presence of polar functional groups (or heteroatoms) regulates this threshold, causing a shift to some extent.

3.2.2. *Effect of moisture content on ·H production*

Under high-temperature hydrous conditions, the transformation of organic compounds involves several reactions, including hydrolysis, pyrolysis, dehydration, hydrogenation, and polymerization. These reactions lead to the production of numerous intermediate products (Wei et al., 2021). The number of inorganic free radicals (Fig. 13(a) and (b)) in the pyrolysis process of shale kerogen in the Longmaxi Formation increases first and then decreases, indicating that a large number of intermediate products and transient free radicals are generated at the initial stage of the reaction, which can enhance the reactivity of the system. In the subsequent stage, the active radicals are annihilated by coupling, leaving relatively stable free radicals. For AY1-6, there is a significant difference in the number of free radicals at different moisture contents, with the medium moisture content groups (1 and 3 wt.%) exhibiting a higher number of free radicals compared to the other groups. In contrast, the free radical yield in AY2 is relatively low, with minimal differences observed between the groups. The 5 wt.% moisture content group exhibits a slightly higher number of free radicals than the other groups. This indicates that water can promote the formation of intermediates and improve the reactivity of the system, and AY1-6 is more sensitive to water molecules and is greatly affected by the difference in moisture content. The cumulative number of distinct inorganic species that appeared throughout the reaction was statistically analyzed. Further analysis shows that this cumulative number of inorganic species is positively correlated with moisture content (Fig. 13(c)). Consistent with this trend, the cumulative variety (number) of inorganic products in the AY1-6 system is significantly higher than in AY2, with the latter reaching only about 50% of the former. This may be due to the lower aromatic condensation degree and higher hydrophilicity of AY1-6, which enable it to undergo more complex reactions in the presence of water, promoting the formation of more kinds of intermediates.

Water is the sole external hydrogen donor in this study, supplying a significant amount of H and OH. In the anhydrous pyrolysis of kerogen, hydrogen free radical (·H) is primarily generated from the dehydrogenation of aromatic rings, cyclization of aliphatic hydrocarbons, aromatization of cycloalkanes, and polycondensation of aromatic and heterocyclic compounds (Jia et al.,

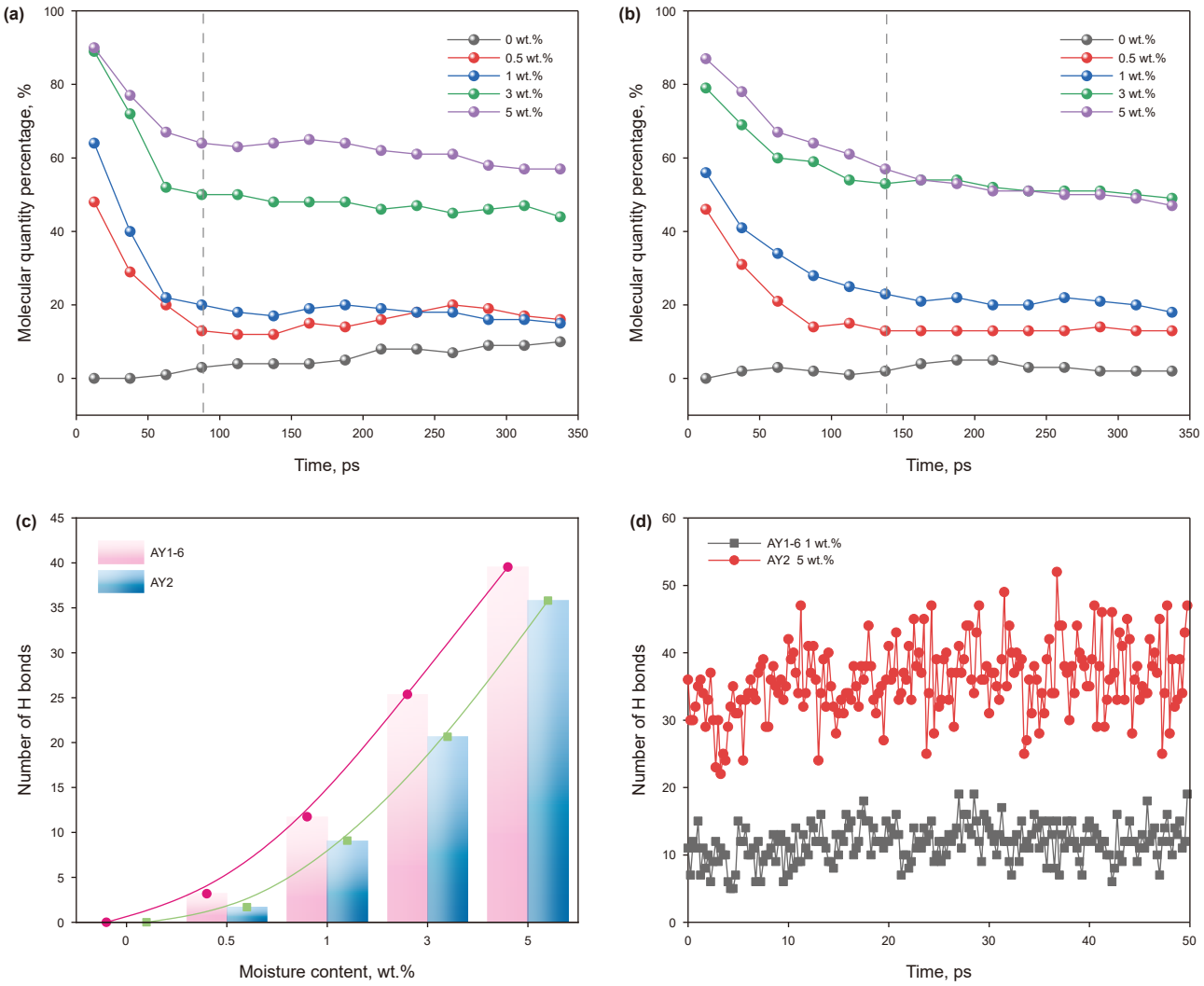

Fig. 12. Comparison of water percentage and hydrogen bond count in AY1-6 and AY2 systems under varying moisture conditions: **(a)** water percentage in AY1-6, **(b)** water percentage in AY2, **(c)** average hydrogen bond count in AY1-6 and AY2 during the relaxation stage, **(d)** hydrogen bond count in the relaxation stage of AY1-6 and AY2 at optimal moisture content threshold for promoting pyrolysis.

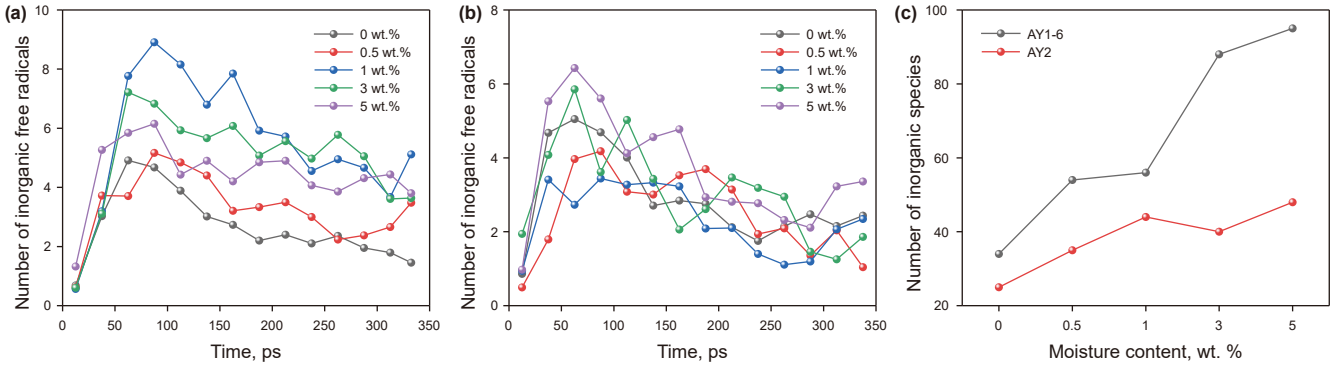

Fig. 13. The changes of the number of inorganic free radicals (**(a)** AY1-6 and **(b)** AY2) and the species statistics **(c)** of inorganic products during the pyrolysis of AY1-6 and AY2 kerogen at different moisture contents.

2015). To enable comparison, and considering that ·OH may convert to ·H at high temperatures (Ding et al., 2025), this study examines the dynamic evolution of ·H. The evolution of ·H concentration (Fig. 14) shows that the hydrogen donation effect of water significantly influences ·H concentration. During the initial stage (0–20 ps), the ·H concentration in the hydrous groups is higher. However, the catalytic effect of water molecules accelerates the cracking of kerogen and the consumption of ·H, resulting

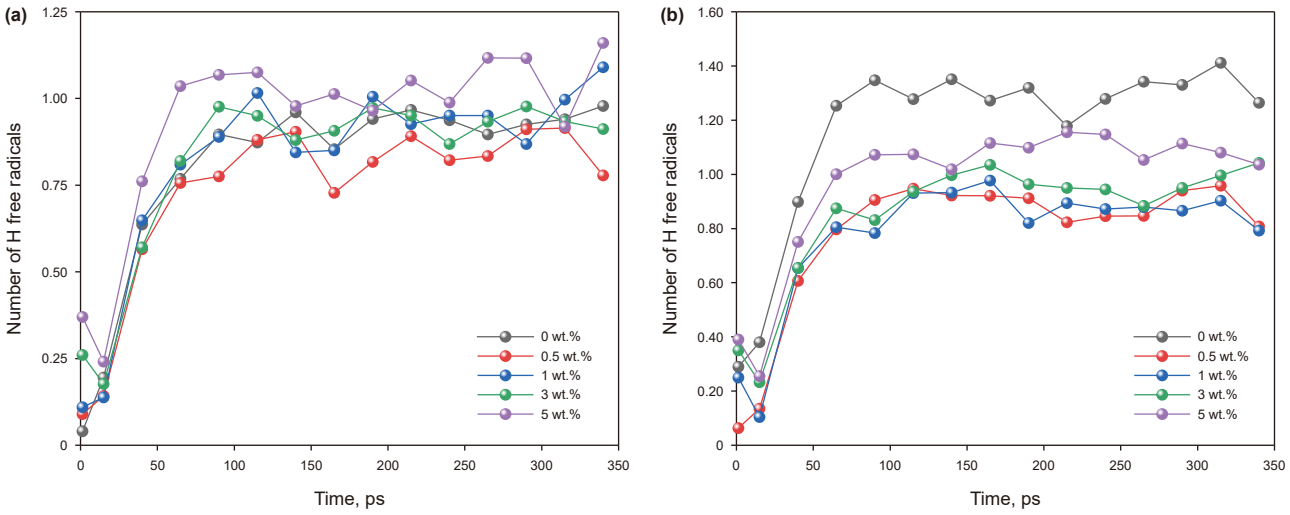

Fig. 14. The number of ·H of AY1-6 **(a)** and AY2 **(b)** in ReaxFF pyrolysis simulation under different moisture content conditions.

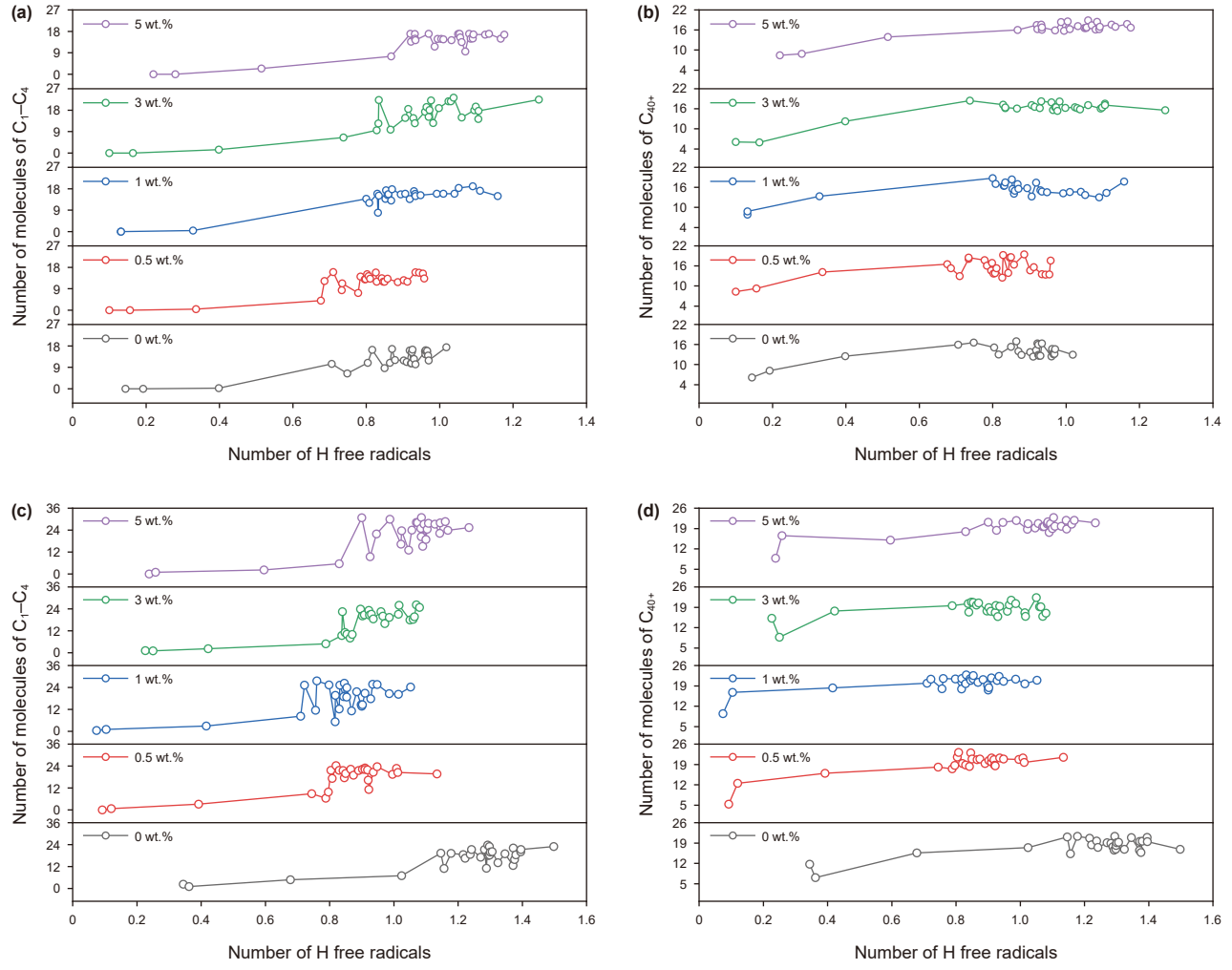

Fig. 15. The yield of gaseous hydrocarbons and char during the pyrolysis of kerogen AY1-6 and AY2 under different moisture content conditions varies with the ·H concentration. Among them, **(a)** and **(b)** are gaseous hydrocarbons (C_1–C_4) and char (C_{40+}) of AY1-6, respectively; **(c)** and **(d)** are gaseous hydrocarbons (C_1–C_4) and char (C_{40+}) of AY2, respectively.

in a significant downward trend in the hydrous groups. After 20 ps, as the temperature increases, the cracking of both water molecules and kerogen intensifies. The formation rate of ·H exceeds the consumption rate, causing its concentration to increase significantly and reach equilibrium around 70 ps. In the AY1-6 system, the ·H concentration is highest in the 5 wt.% moisture content group, whereas in AY2 it reaches its highest value during anhydrous pyrolysis. The instantaneous concentration of ·H reflects the relative rates of its formation and consumption. This phenomenon occurs because water molecules can dissociate to generate a large amount of ·H, while also accelerating the consumption of ·H through the formation of H_2 or by hydrogenating organic macromolecules. In the anhydrous pyrolysis of kerogen, the pyrolysis primarily focuses on the dehydrogenation and condensation of kerogen molecules, directly releasing ·H. Additionally, the slower kerogen cracking rate results in less ·H consumption, leading to some accumulation of ·H. Therefore, the ·H concentration in the hydrous system does not have a clear advantage over the anhydrous system and may even be lower.

As shown in Fig. 15, the yield of gaseous hydrocarbons and char in kerogen is positively correlated with the concentration of ·H. As the concentration of ·H increases, the yields of gaseous hydrocarbons and char generally rise. This may be because ·H are released during kerogen cracking. As a carrier of chain reaction transmission, ·H promotes the reaction, thereby increasing the overall hydrocarbon generation, resulting in an increase in free radical concentration and an increase in hydrocarbon production. However, a high ·H concentration does not necessarily lead to a high yield. The highest ·H yield for AY1-6 and AY2 is observed in the 5 wt.% moisture content group and the anhydrous group, respectively. Their highest gaseous hydrocarbon yields are found in the 1 and 5 wt.% moisture content groups. This phenomenon of high ·H concentration but low hydrocarbon yield can be attributed to the following factors. Firstly, an excessively high ·H concentration increases the likelihood of the $H\cdot + H\cdot \rightarrow H_2$ reaction, which reduces the efficiency of ·H coupling with carbon free radicals (R·) to form hydrocarbons. This is validated in AY1-6: when averaging the H_2 yield after 80 ps, the quantities of H_2 produced for the groups with moisture contents of 1, 3, and 5 wt.% are 1.00, 2.92, and 3.99, respectively. The H_2 yield increases significantly with rising ·H concentration, indicating that a substantial amount of ·H is consumed. This consumption leads to a locally "hydrogen-deficient" environment, which in turn promotes condensation reactions and the formation of macromolecular structures. Secondly, kerogen with a high degree of aromatic condensation (e.g., AY2) forms a dense structure. In the absence of water, high concentrations of external ·H struggle to penetrate the internal carbon skeleton, causing an internal "hydrogen deficiency" that favors intramolecular or intermolecular condensation reactions.

4. Conclusion

In this study, we construct a molecular model of the Silurian kerogen from Guizhou based on elemental analysis, FTIR, ^{13}C-NMR, and XPS tests. The effects of different moisture contents on the pyrolysis of shale organic matter with different aromatic condensation degrees in Longmaxi Formation are discussed from the molecular point of view. The main conclusions include.

(1) The total energy and potential energy of kerogen system increased with the increase of moisture content. It shows that during the evolution of shale hydrocarbon generation, the hydrous system needs more energy to reach the target pyrolysis temperature and increase the pyrolysis time. Moreover, kerogen with a higher degree of aromatic compound condensation requires more energy to be heated to the same temperature. Even under the same pyrolysis conditions, these kerogens have a slower reaction rate and longer reaction time, but their gaseous hydrocarbon yield is higher.

(2) During the pyrolysis process, the yield of gaseous hydrocarbons increases steadily, while the yield of char rises initially and then decreases. Compared to anhydrous pyrolysis, hydrous pyrolysis at high temperature not only promotes the cracking of kerogen and increases the yield of gaseous hydrocarbons, but also enhances the saturation of the hydrocarbon products. The degree of aromatic condensation in kerogen plays a key role in determining the optimal moisture content threshold for pyrolysis: the higher the degree of aromatic condensation, the higher the threshold. However, when the free radicals provided by water are insufficient to compensate for the free radicals consumed during the process, this may inhibit the cracking reaction of the kerogen.

(3) As the pyrolysis temperature and time increase, the number of inorganic free radicals in the pyrolysis products initially increases and then decreases. Water molecules promote the formation of intermediates and transient free radicals and improve the reactivity. Kerogen with a low degree of aromatic condensation is more susceptible to water, exhibiting stronger reactivity. The yields of gaseous hydrocarbons and char in kerogen are positively correlated with the concentration of ·H.

CRediT authorship contribution statement

Yue-Qin Li: Writing – review & editing, Writing – original draft, Software, Methodology, Investigation, Formal analysis, Conceptualization. **Wen-Ji-Bin Sun:** Writing – review & editing, Funding acquisition. **Yu-Jun Zuo:** Supervision. **Bo-Bo Li:** Methodology. **Zhong-Hu Wu:** Resources, Investigation. **Lei Zhang:** Software, Data curation. **Ren-Jun Tian:** Software, Investigation. **Wei Lv:** Software, Investigation.

Data availability

The datasets generated during and/or analyzed during the current study are available from the corresponding author on reasonable request.

Declaration of competing interest

The authors declare that they have no known competing financial interests or personal relationships that could have appeared to influence the work reported in this paper.

Acknowledgments

This study was financially supported by grants from the National Natural Science Foundation of China (under Grant Nos. 52264004, 52374118, 52464004 and 52464010), the Guizhou Provincial fundamental study schedule (Natural Science, Project No. Qiankehe Basic-ZK [2024] General 050 and Qiankehe Support [2025] General 080), the Guizhou Provincial Science and Technology Support Program (Project [2025] General 078) and the

Guizhou Outstanding Young Science and Technology Talent Program (YQK [2023]012).

References

Atmani, L., Bichara, C., Pellenq, R.J.-M., et al., 2017. From cellulose to kerogen: molecular simulation of a geological process. Chem. Sci. 8 (12), 8325–8335. https://doi.org/10.1039/C7SC03466K.

Babaei, S., Ghasemzadeh, H., Tesson, S., 2023. Methane adsorption of nanocomposite shale in the presence of water: insights from molecular simulations. Chem. Eng. J. 475, 146196. https://doi.org/10.1016/j.cej.2023.146196.

Behar, F., Lewan, M.D., Lorant, F., et al., 2003. Comparison of artificial maturation of lignite in hydrous and nonhydrous conditions. Org. Geochem. 34 (4), 575–600. https://doi.org/10.1016/S0146-6380(02)00241-3.

Castro-Marcano, F., Kamat, A.M., Russo, M.F., et al., 2012. Combustion of an illinois no. 6 coal char simulated using an atomistic char representation and the ReaxFF reactive force field. Combust. Flame 159 (3), 1272–1285. https://doi.org/10.1016/j.combustflame.2011.10.022.

Chen, B., Zhang, Y.X., Shi, H.C., et al., 2026. Complex reaction processes in kerogen pyrolysis unraveled by deep learning-based molecular dynamics simulation. J. Anal. Appl. Pyrolysis 193, 107341. https://doi.org/10.1016/j.jaap.2025.107341.

Chen, K.X., Li, J., Zhang, Y.X., et al., 2025a. The impact of different functional groups of biochar on mercury adsorption investigated by density functional theory. J. Clean. Prod. 486, 144546. https://doi.org/10.1016/j.jclepro.2024.144546.

Chen, K.X., Zhang, Y.X., Chen, B., 2025b. Structural characterization and pyrolysis mechanism of γ-O-4 in lignin unraveled by density functional theory simulation. Fuel 379, 133065. https://doi.org/10.1016/j.fuel.2024.133065.

Chen, Y.Z., Wang, Z.T., Li, B., et al., 2023. ReaxFF molecular dynamics study on the microscopic mechanism for kerogen pyrolysis. Langmuir 39 (50), 18581–18593. https://doi.org/10.1021/acs.langmuir.3c02908.

Cheng, P., Xiao, X.M., Wang, X., et al., 2019. Evolution of water content in organic-rich shales with increasing maturity and its controlling factors: implications from a pyrolysis experiment on a water-saturated shale core sample. Mar. Petrol. Geol. 109, 291–303. https://doi.org/10.1016/j.marpetgeo.2019.06.023.

Cypres, R., 1987. Aromatic hydrocarbons formation during coal pyrolysis. Fuel Process. Technol. 15, 1–15. https://doi.org/10.1016/0378-3820(87)90030-0.

Ding, W., Takahashi, O., Wang, J., et al., 2025. A study on free radical behaviors and reactions in supercritical water using quantum chemical simulation. J. Mol. Liq. 419, 126791. https://doi.org/10.1016/j.molliq.2024.126791.

Gao, J., Ni, Y.Y., Li, W., et al., 2020. Pyrolysis of coal measure source rocks at highly to over mature stage and its geological implications. Petrol. Explor. Dev. 47 (4), 773–780. https://doi.org/10.1016/S1876-3804(20)60092-1.

Guo, Y., Tian, G., Chang, X.L., et al., 2024. ReaxFF-based molecular dynamics study of the mechanism of the reaction of N2O4 with H2O. ACS Omega 9 (17), 8. https://doi.org/10.1021/acsomega.3c08695.

Han, Q., Deng, C.B., Gao, T., et al., 2023. Construction of different metamorphic degree coal models and corresponding adsorption characteristics based on molecular simulation. J. Mol. Struct. 1274, 134517. https://doi.org/10.1016/j.molstruc.2022.134517.

He, J.Q., Li, X.Y., Li, Z.L., et al., 2023. The molecular evolution mechanism of direct pyrolysis and hydropyrolysis of changqing petroleum coke was compared based on ReaxFF method. J. Mol. Struct. 1290, 135882. https://doi.org/10.1016/j.molstruc.2023.135882.

Hou, D.L., Qiu, X.D., Gong, F.M., et al., 2023. Characterization of kerogen molecular structure and its effect on methane adsorption behavior: a comparative study on outcrop and core samples from longmaxi shale. Chem. Eng. J. 466, 143293. https://doi.org/10.1016/j.cej.2023.143293.

Hou, H.D., Yang, W., Yang, R., et al., 2025. Formation and evolution of complex pore-fracture systems in shale gas reservoirs: insights into controlling mechanisms. Energy Fuels. 39 (6), 3008–3038. https://doi.org/10.1021/acs.energyfuels.4c05306.

Hu, D.J., Li, Z.X., Liu, Y., et al., 2024. Coal pyrolysis law and mechanism of index gas generation in linsheng mine. J. Mol. Struct. 1297, 136912. https://doi.org/10.1016/j.molstruc.2023.136912.

Hu, E.F., Zeng, X., Ma, D.C., et al., 2017. Effect of the moisture content in coal on the pyrolysis behavior in an indirectly heated fixed-bed reactor with internals. Energy Fuels. 31 (2), 1347–1354. https://doi.org/10.1021/acs.energyfuels.6b02780.

Huang, L., Ning, Z.F., Wang, Q., et al., 2018. Molecular simulation of adsorption behaviors of methane, carbon dioxide and their mixtures on kerogen: effect of kerogen maturity and moisture content. Fuel 211, 159–172. https://doi.org/10.1016/j.fuel.2017.09.060.

Huang, L., Ning, Z.F., Wang, Q., et al., 2017. Thermodynamic and structural characterization of bulk organic matter in Chinese silurian shale: experimental and molecular modeling studies. Energy Fuels. 31 (5), 4851–4865. https://doi.org/10.1021/acs.energyfuels.7b00132.

Huang, Z.B., Zhou, W.J., Wei, J.J., 2023. Study on the molecular structure model of tar-rich coal and its pyrolysis process. J. Mol. Struct. 1286, 135613. https://doi.org/10.1016/j.molstruc.2023.135613.

Iglesias, M.J., Jimenez, A., Laggoun-Defarge, F., et al., 1995. FTIR study of pure vitrains and associated coals. Energy Fuels. 9 (3), 458–466. https://doi.org/10.1021/ef00051a010.

Jagadisan, A., Heidari, Z., 2019. Experimental quantification of the effect of thermal maturity of kerogen on its wettability. SPE Reservoir Eval. Eng. 22 (4), 1323–1333. https://doi.org/10.2118/195684-PA.

Jia, C.X., Wang, Z.C., Liu, H.P., et al., 2015. Pyrolysis behavior of Indonesia oil sand by TG-FTIR and in a fixed bed reactor. J. Anal. Appl. Pyrolysis 114, 250–255. https://doi.org/10.1016/j.jaap.2015.06.003.

Kelemen, S.R., Afeworki, M., Gorbaty, M.L., et al., 2007. Direct characterization of kerogen by X-ray and solid-state 13 C nuclear magnetic resonance methods. Energy Fuels. 21 (3), 1548–1561. https://doi.org/10.1021/ef060321h.

Lawal, L.O., Olayiwola, T., Abdel-Azeim, S., et al., 2020. Molecular simulation of kerogen-water interaction: theoretical insights into maturity. J. Mol. Liq. 299, 112224. https://doi.org/10.1016/j.molliq.2019.112224.

Lewan, M.D., 1997. Experiments on the role of water in petroleum formation. Geochem. Cosmochim. Acta 61 (17), 3691–3723. https://doi.org/10.1016/S0016-7037(97)00176-2.

Lewan, M.D., Winters, J.C., McDonald, J.H., 1979. Generation of oil-like pyrolyzates from organic-rich shales. Science 203 (4383), 897–899. https://doi.org/10.1126/science.203.4383.897.

Li, G.X., Zheng, F.J., Huang, Q.F., et al., 2022. Molecular insight into pyrolysis processes via reactive force field molecular dynamics: a state-of-the-art review. J. Anal. Appl. Pyrolysis 166, 105620. https://doi.org/10.1016/j.jaap.2022.105620.

Li, J., Ning, Z.F., Li, Q., et al., 2025. A molecular simulation model for kerogen reconstruction and methane adsorption under slickwater exposure. Langmuir 41 (29), 19240–19251. https://doi.org/10.1021/acs.langmuir.5c01635.

Li, S.D., Wei, Z.W., Liu, H., et al., 2022. A new method for the quantification of hydrogen contribution from water to methane during hydrous kerogen pyrolysis. Org. Geochem. 173, 104495. https://doi.org/10.1016/j.orggeochem.2022.104495.

Lindsey, D.R., Rimmer, S.M., Anderson, K.B., 2023. Modified open-system hydrous pyrolysis. Int. J. Coal Geol. 275, 104313. https://doi.org/10.1016/j.coal.2023.104313.

Liu, C.J., Lu, J.Y., Zheng, F., et al., 2024. Molecular structure model construction and pyrolysis mechanism study on low-rank coal by experiments and ReaxFF simulations. J. Anal. Appl. Pyrolysis 178, 106387. https://doi.org/10.1016/j.jaap.2024.106387.

Liu, Y., Liu, S.M., Zhang, R., et al., 2021. The molecular model of marcellus shale kerogen: experimental characterization and structure reconstruction. Int. J. Coal Geol. 246, 103833. https://doi.org/10.1016/j.coal.2021.103833.

Liu, Y.Q., Yao, C.J., Meng, X.X., et al., 2024. Pyrolysis mechanism and reservoir simulation study of organic-rich shale during the in situ conversion via supercritical water heating. Energy Fuels. 38 (15), 14246–14261. https://doi.org/10.1021/acs.energyfuels.4c02100.

Luzar, A., Chandler, D., 1993. Structure and hydrogen bond dynamics of water–dimethyl sulfoxide mixtures by computer simulations. J. Chem. Phys. 98 (10), 8160–8173. https://doi.org/10.1063/1.464521.

Meng, F.Y., Yao, C.J., Yang, H.C., et al., 2024. Changes of the multiscale pore structure and connectivity of organic-rich shale during hydrous pyrolysis under different temperatures and pressures. Energy Fuels. 38 (18), 17554–17570. https://doi.org/10.1021/acs.energyfuels.4c02778.

Michels, R., Landis, P., Philp, R.P., et al., 1995. Influence of pressure and the presence of water on the evolution of the residual kerogen during confined, hydrous, and high-pressure hydrous pyrolysis of woodford shale. Energy Fuels. 9 (2), 204–215. https://doi.org/10.1021/ef00050a002.

Okiongbo, K.S., Aplin, A.C., Larter, S.R., 2005. Changes in type II kerogen density as a function of maturity: evidence from the kimmeridge clay formation. Energy Fuels. 19 (6), 2495–2499. https://doi.org/10.1021/ef050194+.

Painter, P.C., Snyder, R.W., Starsinic, M., et al., 1981. Concerning the application of FT-IR to the study of coal: a critical assessment of band assignments and the application of spectral analysis programs. Appl. Spectrosc. 35 (5), 475–485. https://doi.org/10.1366/0003702814732256.

Pan, S., Zhou, H.Y., Wang, Q., et al., 2022. Experimental and molecular simulation studies of huadian oil shale kerogen. ACS Omega 7 (20), 17253–17269. https://doi.org/10.1021/acsomega.2c01174.

Pinder, J.W., Major, G.H., Baer, D.R., et al., 2024. Avoiding common errors in X-ray photoelectron spectroscopy data collection and analysis, and properly reporting instrument parameters. Appl. Surf. Sci. Adv. 19, 100534. https://doi.org/10.1016/j.apsadv.2023.100534.

Pitera, J.W., 2014. Expected distributions of root-mean-square positional deviations in proteins. J. Phys. Chem. B. 118 (24), 6526–6530. https://doi.org/10.1021/jp412776d.

Qiu, Y., Zhong, W.Q., Yu, A.B., 2022. Simulations on pressurized oxy-coal combustion and gasification by molecular dynamics method with ReaxFF. Adv. Powder Technol. 33 (5), 103557. https://doi.org/10.1016/j.apt.2022.103557.

Roshan, H., Al-Yaseri, A.Z., Sarmadivaleh, M., et al., 2016. On wettability of shale rocks. J. Colloid Interface Sci. 475, 104–111. https://doi.org/10.1016/j.jcis.2016.04.041.

Salmon, E., Van Duin, A.C.T., Lorant, F., et al., 2009. Thermal decomposition process in algaenan of botryococcus braunii race L. part 2: molecular dynamics simulations using the ReaxFF reactive force field. Org. Geochem. 40 (3), 416–427. https://doi.org/10.1016/j.orggeochem.2008.08.012.

Sanchouli, N., Babaei, S., Kanduč, M., et al., 2024. Wetting behavior of kerogen surfaces: insights from molecular dynamics. Langmuir 40 (11), 5715–5724. https://doi.org/10.1021/acs.langmuir.3c03367.

Siskin, M., Katritzky, A.R., 1991. Reactivity of organic compounds in hot water: geochemical and technological implications. Science 254 (5029), 231–237. https://doi.org/10.1126/science.254.5029.231.

Su, R.K., Xue, R.Q., Ma, X.C., et al., 2024. Targeted improvement of narrow micropores in porous carbon for enhancing trace benzene vapor removal: revealing the adsorption mechanism via experimental and molecular simulation. J. Colloid Interface Sci. 671, 770–778. https://doi.org/10.1016/j.jcis.2024.05.165.

Sun, B., Liu, X.P., Liu, J., et al., 2025. Evolution and generation mechanism of retained oil in lacustrine shales: a combined ReaxFF-MD and pyrolysis simulation perspective. Pet. Sci. 22 (1), 29–41. https://doi.org/10.1016/j.petsci.2024.07.020.

Trewhella, M.J., Poplett, I.J.F., Grint, A., 1986. Structure of green river oil shale kerogen. Fuel 65 (4), 541–546. https://doi.org/10.1016/0016-2361(86)90046-3.

Ungerer, P., Collell, J., Yiannourakou, M., 2015. Molecular modeling of the volumetric and thermodynamic properties of kerogen: influence of organic type and maturity. Energy Fuels. 29 (1), 91–105. https://doi.org/10.1021/ef502154k.

Wang, D.T., Seewald, J.S., Reeves, E.P., et al., 2022a. Incorporation of water-derived hydrogen into methane during artificial maturation of source rock under hydrothermal conditions. Org. Geochem. 171, 104468. https://doi.org/10.1016/j.orggeochem.2022.104468.

Wang, L.Y., Yao, Q.X., Cao, R., et al., 2024. Mechanism of phenols evolution during pyrolysis of shendong coal macerals swelled with oxygen-containing organic solvents: experimental and DFT study. Chem. Eng. J. 493, 152648. https://doi.org/10.1016/j.cej.2024.152648.

Wang, Q., Wang, X.M., Pan, S., 2022b. The three-dimensional molecular structure model of fushun oil shale kerogen. China. J. Mol. Struct. 1255, 132380. https://doi.org/10.1016/j.molstruc.2022.132380.

Wang, X.M., Wang, Q., Pan, S., et al., 2023. The non-isothermal thermal decomposition evolution of the fushun oil shale kerogen based on ReaxFF molecular dynamics simulation. J. Anal. Appl. Pyrolysis 169, 105869. https://doi.org/10.1016/j.jaap.2023.105869.

Wang, R.Y., Gu, Y., Ding, W.L., et al., 2016. Characteristics and dominant controlling factors of organic-rich marine shales with high thermal maturity: a case study of the lower cambrian niutitang formation in the cen'gong block, southern China. J. Nat. Gas Sci. Eng. 33, 81–96. https://doi.org/10.1016/j.jngse.2016.05.009.

Wang, R.Y., Wang, G.P., Zhao, G., et al., 2023. Geological characteristics and resources potential of shale oil in chang 7 member of upper triassic yanchang formation in fuxian area, southern ordos basin, Western China. Unconventional Resources 3, 237–247. https://doi.org/10.1016/j.uncres.2023.06.001.

Wang, X.H., Huang, X.F., Lin, K., et al., 2019. The constructions and pyrolysis of 3D kerogen macromolecular models: experiments and simulations. Glob. Chall. 3 (5), 1900006. https://doi.org/10.1002/gch2.201900006.

Wang, X.F., Liu, W.H., Xu, Y.C., et al., 2011. Influences of water media on the hydrogen isotopic composition of natural gas/methane in the processes of gaseous hydrocarbon generation and evolution. Sci. China Earth Sci. 54 (9), 1318–1325. https://doi.org/10.1007/s11430-011-4195-0.

Wei, N., Xu, D.H., Hao, B.T., et al., 2021. Chemical reactions of organic compounds in supercritical water gasification and oxidation. Water Res. 190, 116634. https://doi.org/10.1016/j.watres.2020.116634.

Yang, J., Yan, Q.R., Deng, L., et al., 2025a. The non-isothermal and isothermal pyrolysis mechanism of longmaxi type II oil shale kerogen: a ReaxFF molecular dynamics study. Fuel 380, 133169. https://doi.org/10.1016/j.fuel.2024.133169.

Yang, W., Xie, M., Hou, H.D., et al., 2025b. Multifractal characteristics of heterogeneous pore-throat structure and insight into differential fluid movability of saline-lacustrine mixed shale-oil reservoirs. Fractal and Fractional 9 (9), 604–640. https://doi.org/10.3390/fractalfract9090604.

Zhang, L.C., Xiao, D.S., Lu, S.F., et al., 2019a. Effect of sedimentary environment on the formation of organic-rich marine shale: insights from major/trace elements and shale composition. Int. J. Coal Geol. 204, 34–50. https://doi.org/10.1016/j.coal.2019.01.014.

Zhang, X., Guo, W., Pan, J.F., et al., 2024. In-situ pyrolysis of oil shale in pressured semi-closed system: insights into products characteristics and pyrolysis mechanism. Energy 286, 129608. https://doi.org/10.1016/j.energy.2023.129608.

Zhang, Z.J., Chai, J., Zhang, H.Y., et al., 2021. Structural model of longkou oil shale kerogen and the evolution process under steam pyrolysis based on ReaxFF molecular dynamics simulation. Energy Sources, Part A Recovery, Util. Environ. Eff. 43 (2), 252–265. https://doi.org/10.1080/15567036.2019.1624879.

Zhang, Z.J., Guo, L.T., Zhang, H.Y., et al., 2019b. Comparing product distribution and desulfurization during direct pyrolysis and hydropyrolysis of longkou oil shale kerogen using reactive MD simulations. Int. J. Hydrogen Energy 44 (47), 25335–25346. https://doi.org/10.1016/j.ijhydene.2019.08.036.

Zhao, F.M., Li, B., Che, D.C., et al., 2023. The mechanism of H2O in the superheated steam affecting the quality of in-situ pyrolysates of oil shale kerogen: part B-favorable conversion of residues. Fuel 337, 127146. https://doi.org/10.1016/j.fuel.2022.127146.

Zhao, F.M., Li, B., Zhang, L., et al., 2022. The mechanism of superheated steam affecting the quality of in-situ pyrolysates of oil shale kerogen: part a-saturation of pyrolytic organics. Fuel 323, 124331. https://doi.org/10.1016/j.fuel.2022.124331.

Zheng, T.Y., Littke, R., Zieger, L., et al., 2023. Kerogen structure and porosity in woodford shale before and after hydrous closed-system pyrolysis. Int. J. Coal Geol. 279, 104375. https://doi.org/10.1016/j.coal.2023.104375.

Zhong, L., Wang, Z.J., Ye, X.H., et al., 2024. Molecular simulations guide immobilization of lipase on nest-like ZIFs with regulatable hydrophilic/hydrophobic surface. J. Colloid Interface Sci. 667, 199–211. https://doi.org/10.1016/j.jcis.2024.04.075.

Zhou, J., Zhang, J.J., Yang, J.P., et al., 2022. Mechanisms for kerogen wettability transition from water-wet to CO_2-wet: implications for CO_2 sequestration. Chem. Eng. J. 428, 132020. https://doi.org/10.1016/j.cej.2021.132020.